

RESEARCH ARTICLE | MARCH 21 2025

Numerical analysis of air entrainment and flows around a surface-piercing finite circular cylinder

Wenbin Zhang (章文彬) ; Minghai Wang (王铭海) ; Weiwen Zhao (赵伟文) ; Decheng Wan (万德成)  



Physics of Fluids 37, 032127 (2025)

<https://doi.org/10.1063/5.0259260>



Articles You May Be Interested In

Numerical investigation of flow structure and air entrainment of breaking bow wave generated by a rectangular plate

Physics of Fluids (December 2021)

Wake and air entrainment properties of transom stern over a wide range of Froude numbers

Physics of Fluids (June 2023)

Numerical Breaking Waves around a Surface Piercing NACA 0012 Hydrofoil

AIP Conference Proceedings (September 2011)



Physics of Fluids

Special Topics Open
for Submissions

[Learn More](#)



Numerical analysis of air entrainment and flows around a surface-piercing finite circular cylinder

Cite as: Phys. Fluids **37**, 032127 (2025); doi: 10.1063/5.0259260

Submitted: 18 January 2025 · Accepted: 27 February 2025 ·

Published Online: 21 March 2025



View Online



Export Citation



CrossMark

Wenbin Zhang (章文彬),  Minghai Wang (王铭海),  Weiwen Zhao (赵伟文),  and Decheng Wan (万德成)^{a)} 

AFFILIATIONS

Computational Marine Hydrodynamics Lab (CMHL), School of Ocean and Civil Engineering, Shanghai Jiao Tong University, Shanghai, China

^{a)} Author to whom correspondence should be addressed: dcwan@sjtu.edu.cn

ABSTRACT

Flows past a surface-piercing finite circular cylinder at various Froude numbers Fr ranging from 0.8 to 1.7 are investigated by utilizing high-fidelity numerical simulation based on the adaptive mesh refinement technique, the geometric volume-of-fluid method, and the embedded boundary method. The primary objective of the study is to reveal the relationship and interactions between the flow field and the air entrainment mechanism in a surface-piercing cylinder flow. Numerical approaches are validated in various aspects by comparing simulation results to previous experimental and numerical data. The detailed flow characteristics, including free surface deformation, velocity fields, and vortex structures at different Froude numbers, are discussed thoroughly. The free surface breaking is captured and characterized by the local surface slope $|\nabla\eta|$, with three distinct breaking regions and two different breaking types identified. Features of the velocity field at various Froude numbers are discovered by analyzing the velocity distributions at certain locations, turbulent kinetic energy, and vortex structures. Bubble statistics including bubble size distribution and spatial distribution are obtained. Three distinct slopes of bubble size distribution $N_r \sim r^{-3/2}, r^{-10/3}, r^{-5}$ are identified for different bubble radius intervals. The bubble spatial distribution is closely related to the Froude number, with the vertical depth of the bubble clouds increasing from $y/D = -1.56$ at $Fr = 1.1$ to $y/D = -2.59$ at $Fr = 1.7$. Many distinct flow characteristics are associated with bubble size and spatial distribution, which can be utilized to interpret air entrainment mechanisms and bubble statistics. Moreover, the effects of surface tension on bubble statistics are examined.

Published under an exclusive license by AIP Publishing. <https://doi.org/10.1063/5.0259260>

I. INTRODUCTION

Flow past a circular cylinder is a hot research topic in fluid mechanics for its wide application in engineering. In the past decades, massive research on the single-phase flow past a circular cylinder has been conducted through experiments^{1–3} and numerical simulations.^{4–7} In terms of ocean engineering, surface-piercing circular cylinders can be simplified models for many marine structures, such as Spar platforms, floating offshore wind turbines, vertical pipes, etc.^{8,9} Understanding the free surface and the finite cylinder interaction provides valuable references for designing relevant marine structures. Early studies on the flow past a surface-piercing finite circular cylinder were conducted by Hay,¹⁰ including more than 350 experiments on various cylinder diameters, depths, and speeds.¹¹ Due to the limitations of measurement and photographic techniques, Hay's studies did not involve detailed characteristics in the free surface deformation and flow field.

In recent years, many experimental and numerical studies on flow past a surface-piercing cylinder were carried out thanks to the

great progress of model basin experimental and high-performance computational technology. Researchers mainly focus on three categories of flow characteristics in this problem.

The first category is the free-surface effect on the forces suffered by the surface-piercing cylinder. Chaplin and Teigen¹² presented an experimental study on surface-piercing cylinders with a constant Reynolds number to Froude number Re/Fr ratio of 2.79×10^5 . They found that the total resistance coefficient peaked at the Froude number of about 1. They also studied the vertical distribution of the resistance force and defined the surface resistance coefficient, which reached a maximum number of 0.9 at the Froude number of about 1. A similar vertical distribution of the drag coefficient was found in the numerical studies by Yu *et al.*¹³ and Koo *et al.*¹⁴ At the Froude number of about 1, the drag coefficient increased from about 0.5 at the bottom of the cylinder to about 1 near the free surfaces. However, the drag coefficients at different vertical positions were almost identical at lower and higher Froude numbers. Benitz *et al.*¹⁵ conducted numerical simulations on surface-piercing circular cylinders of varying aspect ratios at

the Froude number $Fr = 0.65$. The total drag coefficient was relatively small at low aspect ratios compared to the fully submerged case. With the increase in the aspect ratio, the drag coefficient gradually approaches that in the fully submerged case.

The second category is the free surface deformation caused by the cylinder, including the bow wave characteristics and the wake characteristics. Kawamura *et al.*¹⁶ presents a study on the turbulent flow around a surface-piercing circular cylinder at a Reynolds number of approximately 2.7×10^4 and Froude numbers of 0.2, 0.5, 0.8 using large eddy simulation (LES). At low Froude numbers ($Fr = 0.2, 0.5$), the surface deformations were small, and the flow near the surface was similar to the single-phase case. However, at $Fr = 0.8$, the generated surface waves were huge and strongly unsteady. Many researchers paid attention to the bow wave height and the depression depth of the cylinder wake.^{10–14,17,18} The definition of the bow wave height D_1 and the depression depth L_0 is shown in Fig. 1. At low Froude numbers ($Fr^2 < 1$) and high Reynolds numbers ($Re/Fr > 10^5$), a classical equation derived from Bernoulli's theory was adopted to predict the bow wave height D_1 : $D_1/D = Fr^2/2$, where D is the diameter of the cylinder. For lower Reynolds numbers, the bow wave height was fitted to a power law: $D_1/D \propto Fr^B$. The parameter B was close to 1 at the lowest Reynolds numbers and increased to 2 as the Reynolds number increased. At higher Froude numbers ($1 < Fr^2 < 10$), the bow wave height tended to be lower than Bernoulli's theory. Keough *et al.*¹⁷ presented a modification of Bernoulli's theory based on towing tank experiments and curve fitting: $D_1 = V^2/2g - C_{diss}V^2$, in which the turbulent dissipation coefficient C_{diss} was fitted to 0.005. At even higher Froude numbers ($Fr^2 > 10$), the bow wave height tended to a stable value due to strong bow wave breaking. The growing trend of the depression depth L_0 is more complicated. Hay's experimental data provided a fitting power law: $L_0/D = 0.286Fr^2$. However, many experimental and numerical studies have demonstrated that the application range of the fitting power law was limited and the mechanisms behind remain unclear. Recently, some studies shifted focus from points and lines to the whole face of the free surface.^{11,19–22} Detailed characteristics of the bow wave and the wake area at various Froude numbers were discussed.

The third category is the turbulent structures around the cylinder and in the wake area. Kawamura *et al.*¹⁶ observed that periodic vortex shedding was attenuated near the free surface at $Fr = 0.8$. Yu *et al.*¹³

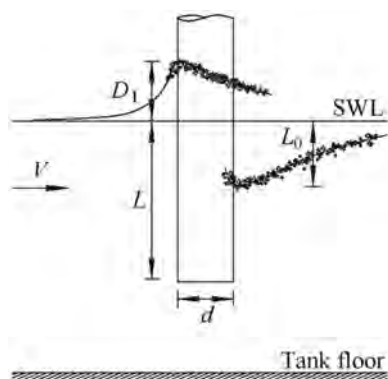


FIG. 1. Definition of bow wave height and depression depth from Chaplin and Teigen.¹²

extended the Froude number up to $Fr = 3$ and the Reynolds number up to $Re = 1 \times 10^5$. The attenuation of organized vortex shedding at the free surface was stronger at higher Froude numbers but reduced at higher Reynolds numbers. Similar observations were found in Suh *et al.*²³ The streamwise vorticity and outward transverse velocity generated at the edge of the separated region were believed to be responsible for the phenomenon. Koo *et al.*¹⁴ conducted a numerical study on the Reynolds and Froude number effects on the flow structures by large eddy simulation and the coupled level-set and volume of fluid (CLSVOF) interfacing capturing method.^{24,25} For the sub-critical Froude number $Fr = 0.84$, smaller bow waves and Kelvin waves were observed, while at $Fr = 1.24$, larger bow waves broke and wrapped around the cylinder, producing splashes and bubbles. At $Fr = 1.64$, bow waves increase significantly, with the largest wake and deepest depression, and Kelvin waves are less visible due to increased turbulence. A remarkably reduced separated region below the interface at $z = -1$ was observed for the critical Re regime, resulting in a much-reduced wake and recirculation region behind the cylinder. Chen *et al.*^{26,27} investigated the flow past a surface-piercing circular and round-cornered square cylinder at $Fr = 1.1$ and $Re = 2.7 \times 10^5$ by delayed detached eddy simulation.^{28,29} The instantaneous and time-averaged primary turbulent structures were thoroughly discussed by using the modified Omega–Liutex method.³⁰ A spectral analysis was further conducted to determine the characteristics of different turbulent structures.

A summary of the previous studies on the flow characteristics past a surface-piercing circular cylinder is listed in Table I.

Recently, some research shed light on the air entrainment and bubbles in the flow past a surface-piercing cylinder at high Froude numbers. Ageorges *et al.*¹⁹ conducted a series of towing tank experiments with the cylinder diameter ranging from 1.4 to 16 cm. The Froude number ranged from 0.2 to 2.4 and the Reynolds number ranged from 4500 to 240 000. Two modes of air entrainment were discovered in the research: (i) in the cavity along the cylinder wall and (ii) in the wake of the cylinder. High-definition optical photos and videos were presented to capture the bubble distribution and trajectories. The flow parameters depicting the different air entrainment regimes were determined based on massive experimental data in various cases. Hilo *et al.*²¹ conducted an experimental study on air ventilation and acoustic characteristics of flow around surface-piercing circular and elliptical cylinders at different Froude numbers. The results showed that the air volume fraction behind the circular cylinder is much higher than the elliptical cylinder due to the formation of the air cavity. The experimental measurements also confirmed that most noise sources behind the cylinder are associated with the air cavity.

However, high-fidelity numerical simulations and analyses on the air entrainment and bubble statistics in the flow past a surface-piercing cylinder at high Froude numbers are limited. How flow characteristics around the surface-piercing finite circular cylinder affect the generation and development of the bubble clouds remains unclear. In addition, the detailed characteristics of the bubble clouds and how they react back to the flow field are of great significance in helping further understand the mechanisms in the surface-piercing finite cylinder flow, especially at high Froude numbers. The present work uses high-fidelity numerical simulations based on the adaptive mesh refinement technique (AMR) to investigate the flow past a surface-piercing finite circular cylinder with bubbles and droplets. The primary objectives are to study the detailed flow and bubble characteristics at high Froude

TABLE I. Summary of the previous studies on three categories of flow characteristics.

Category	Related references	Key characteristics
Drag forces	Chaplin and Teigen; ¹² Yu <i>et al.</i> ; ¹³ Koo <i>et al.</i> ; ¹⁴ Benitz <i>et al.</i> ; ¹⁵ Ageorges <i>et al.</i> ¹⁹	The drag force is reduced compared to the single-phase case. At $Fr = 1$, the drag coefficient peaks near the free surface and varies along the vertical direction.
Free surface deformation	Keough <i>et al.</i> ; ¹¹ Chaplin and Teigen; ¹² Yu <i>et al.</i> ; ¹³ Koo <i>et al.</i> ; ¹⁴ Potts <i>et al.</i> ; ¹⁸ Ageorges <i>et al.</i> ²⁰	The bow wave height is estimated using Bernoulli's theory and its modifications. Different flow regimes in the bow wave and wake area are identified as the increase of the Froude number.
Turbulent structures	Yu <i>et al.</i> ; ¹³ Suh <i>et al.</i> ; ²³ Koo <i>et al.</i> ; ¹⁴ Kawamura <i>et al.</i> ; ¹⁶ Ageorges <i>et al.</i> ; ²⁰ Chen <i>et al.</i> ²⁶	The vortex shedding is attenuated by the free surface, which is replaced by small-scale vortex structures. The two shear layers deviate from the symmetric vertical plane, and the separation region increases in the streamwise and transverse directions.

numbers and to analyze the relationship between air entrainment and flow features. Table II compares the present work with recent research on the flow past a surface-piercing cylinder.

The structure of this paper is as follows: Sec. I gives an introduction to the background and primary focus of the present study. Section II introduces the key computational methods used in the numerical analysis. Section III describes the numerical setup including the physical model, computational domain, and computational mesh. Validations on the numerical approaches are also included. The flow characteristics past a single surface-piercing cylinder at various Froude numbers are discussed and compared to previous studies in Sec. IV. Section V focuses on air entrainment and bubble statistics, including the bubble size distribution, bubble spatial distribution, and the capillary effects on bubble statistics. By relating the features of bubble statistics in Sec. V to the flow features in Sec. IV, the interactions between the flow and air entrainment are investigated and discussed. In the end, the conclusions are summarized in Sec. VI.

II. COMPUTATIONAL METHODS

A. Governing equations

Basilisk³¹ is an open-source solver for solving partial differential equations on adaptive Cartesian meshes, which is the successor of the

famous flow solver Gerris.^{32,33} In this study, the incompressible two-phase Navier–Stokes equations considering surface tension are solved using Basilisk. The governing equations for incompressible two-phase flow are as follows:

$$\begin{cases} \rho \left[\frac{\partial \mathbf{u}}{\partial t} + \mathbf{u}(\nabla \cdot \mathbf{u}) \right] = -\nabla p + \mu \nabla^2 \mathbf{u} + \rho \mathbf{g} + \sigma \kappa \delta_s \mathbf{n}, \\ \frac{\partial \rho}{\partial t} + \nabla \cdot (\rho \mathbf{u}) = 0, \end{cases} \quad (1)$$

where ρ is the density of fluid, $\mathbf{u} = (u, v, w)$ is the velocity vector of fluid, p is pressure, and μ is the fluid dynamic viscosity. The term $\sigma \kappa \delta_s \mathbf{n}$ is introduced for surface tension where σ is the surface tension coefficient, κ and \mathbf{n} are the curvature and normal unit vector to the interface, and the surface Dirac function δ_s helps distinguish the fluid interface. It equals one on the interface and zero otherwise.

For the multiphase flow, an indicator function α is used to locate the air–water interface. The evolution of the interface is given by the following advection equation:

$$\frac{\partial \alpha}{\partial t} + \nabla \cdot (\alpha \mathbf{u}) = 0. \quad (2)$$

TABLE II. Comparison of the present work with recent research on flow past a surface-piercing cylinder.

Reference	Approach (exp./num.)	Fr/Re range	Focus and key findings
Ageorges <i>et al.</i> ¹⁹	exp.	$Fr = 0.2-2.4$ $Re = 4.5 \times 10^3-2.4 \times 10^5$	Uncover two modes of air entrainment and determine the air entrainment onset
Chen <i>et al.</i> ²⁶	num.	$Fr = 1.1$ $Re = 2.7 \times 10^5$	Identify and characterize the turbulent structures; determine the prominent frequency of the turbulent structures
Hilo <i>et al.</i> ²¹	exp.	$Fr = 0.87-1.73$	Air entrainment visualization and air volume calculation; discover the relationship between bubbles and noises
Keough <i>et al.</i> ¹¹	exp.	$Fr = 0.36-3.99$	Characterize the flow regimes under various Froude numbers
Present work	num.	$Fr = 0.8-1.7$ $Re = 2.4 \times 10^4-5.2 \times 10^4$	Characterize the flow features and detailed bubble statistics; reveal the links between flow features, wave breaking, and air entrainment process; discover the surface tension effect on air entrainment and bubbles

B. Interface-capturing method

The momentum-conserving geometric volume of fluid method³⁴ based on piecewise-linear interface calculation (PLIC)³⁵ is employed to precisely capture the discontinuous interface and resolve the small flow structures like bubbles and droplets. The fraction function $f(\mathbf{x}, t)$ is introduced as the volume fraction of water in each cell as follows:

$$f(\mathbf{x}, t) = \frac{1}{V} \int_{\Omega_f} \alpha(\mathbf{x}, t) dV, \tag{3}$$

where \mathbf{x}, t are the position and time of a cell in the simulation.

Then, the evolution advection equation of the interface is discretized as

$$\frac{\partial f}{\partial t} + \mathbf{u} \cdot \nabla f = 0. \tag{4}$$

The density and viscosity of a cell can be written as

$$\begin{cases} \rho(\mathbf{x}, t) = f(\mathbf{x}, t)\rho_w + (1 - f(\mathbf{x}, t))\rho_a, \\ \mu(\mathbf{x}, t) = f(\mathbf{x}, t)\mu_w + (1 - f(\mathbf{x}, t))\mu_a, \end{cases} \tag{5}$$

where $\rho_w, \rho_a, \mu_w,$ and μ_a are the density and the dynamic viscosity of water and air.

The PLIC method is employed to reconstruct the interface. The three-dimensional cell is cut by a plane Γ_f into two parts, the water phase on one side and air on the other. The normal vector of the plane \mathbf{n}_{Γ_f} is estimated using the Mixed-Youngs-Centered method.³⁶ Then the intersection points between the plane Γ_f and the mesh cell boundary ($A, B,$ and C in Fig. 2) are calculated using a predefined stencil with the normal vector \mathbf{n}_{Γ_f} and the volume fraction f as

$$\alpha_{\Gamma_f} = F(\mathbf{n}_{\Gamma_f}, f). \tag{6}$$

C. Embedded boundary method (EBM)

To account for the curved boundary in the Cartesian grid, the embedded boundary method (EBM)^{37,38} is introduced. EBM, also known as the cut-cell method, uses an approach similar to the geometric PLIC method to achieve a sharp solid interface. The cell is also cut by a plane in EBM. Different from PLIC in the g-VOF method, the solid volume fraction of a mixed cell C_S is to be solved. The normal

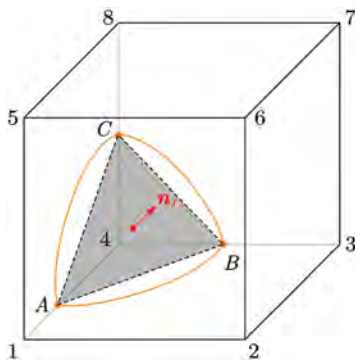


FIG. 2. An example of geometry reconstruction of the interface (solid line: edges of the three-dimensional mesh cell; colored solid line: actual interface; dashed line: reconstructed interface).

vector of the solid interface \mathbf{n}_{Γ_S} and the intersection points are calculated by the predefined geometry. By reversing the same stencil in Sec. II A, the solid volume fraction C_S is calculated as

$$C_S = F^{-1}(\mathbf{n}_{\Gamma_S}, \alpha_S). \tag{7}$$

To achieve the Dirichlet boundary condition and calculate the flux through and the force on the surface of the circular cylinder, the key procedure is to calculate the gradient along the normal vector \mathbf{n}_{Γ_S} of the embedded boundary. A 3D implementation by Schwartz *et al.*³⁸ is adopted as follows:

$$\frac{\partial \phi}{\partial \mathbf{n}} = \frac{1}{d_2 - d_1} \left[\frac{d_2}{d_1} (\phi^B - \phi_1^I) - \frac{d_1}{d_2} (\phi^B - \phi_2^I) \right], \tag{8}$$

where ϕ^B is the value of ϕ on the solid boundary. $\phi_1^I, \phi_2^I,$ are the values of ϕ on the two points for gradient interpolation, respectively. d_1, d_2 are the distances between the solid boundary and the two points. The values of ϕ_1^I, ϕ_2^I are calculated using the biquadratic interpolation with 9 values on the cell center (shown in Fig. 3).

D. Adaptive mesh refinement

As implemented in the Basilisk solver, the tree-based adaptive mesh refinement technique (AMR) plays a crucial role in enhancing the accuracy of numerical simulations while conserving computational resources. This method dynamically adjusts the mesh cell size throughout the simulation, allowing for a more detailed examination of small-scale flow structures such as bubbles and droplets, which are critical in this study.

The AMR module in Basilisk is underpinned by wavelet analysis, which provides a sophisticated approach to grid refinement and coarsening. Wavelet analysis is rooted in multi-resolution analysis and allows for estimating numerical errors in the representation of spatially discretized fields. This study uses the gradient of the velocity field and the volume fraction field for wavelet analysis. When the gradient of the velocity field or the volume fraction field of water reaches a predefined threshold, the parent cell is refined into eight child cells (shown in Fig. 4).

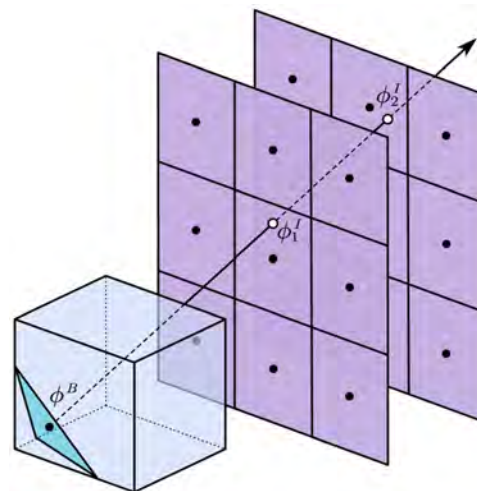


FIG. 3. An example of the second-order stencil for the gradient normal to the interface.

22 March 2025 20:10:18

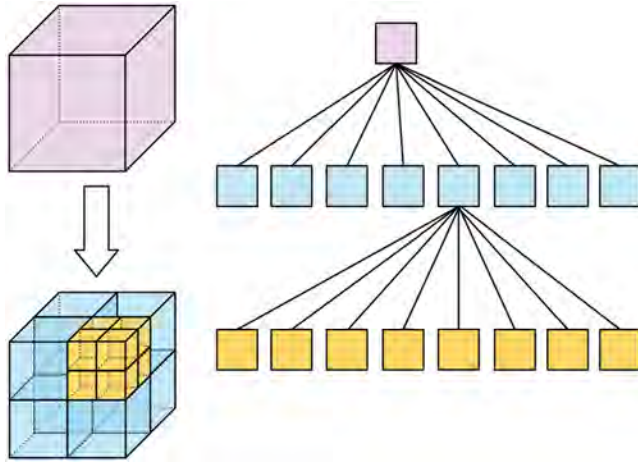


FIG. 4. Octree adaptive mesh refinement.

III. NUMERICAL SETUP

A. Physical model and computational domain

This paper simulates and studies flow past a surface-piercing cylinder at various Froude numbers. The diameter of the cylinder D is equal to 0.05 m, with the draught of the cylinder $h = 2.55D$ and the length of the cylinder $L = 4.55D$. The origin of the computational domain is located at the center of the waterplane of the cylinder. To avoid wall effects and potential fake wave reflections, the size of the computational domain is set to $-10 \leq x/D \leq 25$ in streamwise, $-15 \leq z/D \leq 15$ in cross-stream, and $-8 \leq y/D \leq 8$ vertically. For the boundary conditions, a uniform inflow is set at the inlet and the Neumann boundary condition for velocity is applied for the outlet. A no-slip Dirichlet boundary condition is set on the surface of the circular cylinder using EBM discussed in Sec. II. A sketch of the computational domain is shown in Fig. 5.

The density ratio of water and air is set to $\rho_w/\rho_a = 1000/1 = 1000$ and the viscosity ratio is set to $\mu_w/\mu_a = 1.14 \times 10^{-3}/1.79 \times 10^{-5} = 63.7$. The gravity acceleration is set to $g = 9.8067 \text{m/s}^2$. The surface tension coefficient σ is controlled by the Bond number $Bo = (\rho_w - \rho_a)gD^2/\sigma$. The inlet velocity U_0 is controlled by Froude number $Fr = U_0/\sqrt{gD}$. In this study, we choose five different cases: $Fr = 0.8, 1.1, 1.3, 1.5, \text{ and } 1.7$.

B. Computational mesh and convergence test

The octree adaptive mesh refinement technique is applied in this study. A mesh convergence study is performed at first with three different maximum refinement levels 8, 9, and 10 (corresponding to $256^3, 512^3, \text{ and } 1024^3$ uniform meshes, respectively) to determine a sufficient mesh resolution and quantify numerical uncertainties. The grid convergence index (GCI) introduced by Celik *et al.*³⁹ is adopted, and the bow wave height D_1/D and the depression depth L_0/D are the chosen flow parameters for quantification. The results are shown in Table III. Parameter $\epsilon_{21} = \psi_2 - \psi_1$ and $\epsilon_{32} = \psi_3 - \psi_2$ are the absolute error, where ψ is the value of the chosen flow parameters, the subscript 1, 2, 3 represents fine, medium, and coarse meshes, respectively. $R = \epsilon_{21}/\epsilon_{32}$ is the convergence ratio. As shown in Table III, the

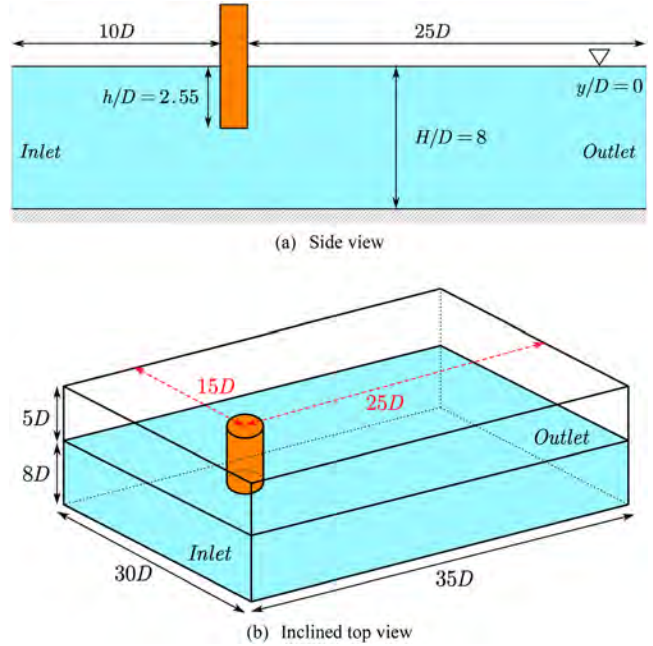


FIG. 5. Sketch of the computational domain.

TABLE III. Mesh convergence study by GCI.

Parameter	ϵ_{21}	ϵ_{32}	R	$GCI_{21}(\%)$	$GCI_{32}(\%)$
D_1/D	-0.0148	-0.0538	0.2749	1.186	4.425
L_0/D	0.0103	-0.0525	-0.1966	0.763	3.977

absolute values of the convergence ratio for both parameters are low, indicating a converged trend. The numerical uncertainties of the fine mesh are $GCI_{21} = 1.186\%, 0.763\%$, indicating a low uncertainty for capturing the free surface characteristics. It is concluded that the fine mesh (maximum refinement level equal to 10) is sufficient for the numerical simulation and analysis.

As the simulation goes, the mesh is adaptively refined or coarsened as needed. Figure 6 shows the instantaneous free surface and the

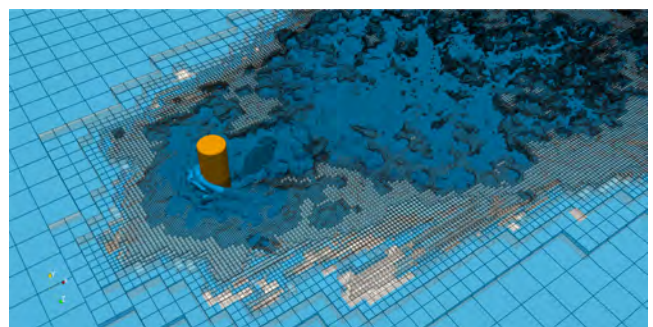


FIG. 6. Adaptive mesh refinement diagram at $t = 3 \text{ s}$.

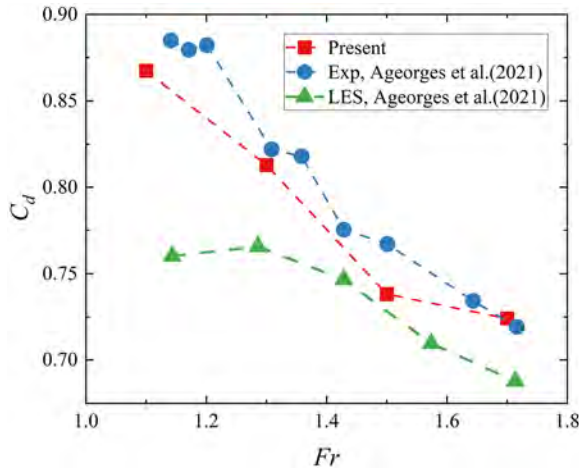


FIG. 7. Drag coefficient C_d at different Froude numbers.

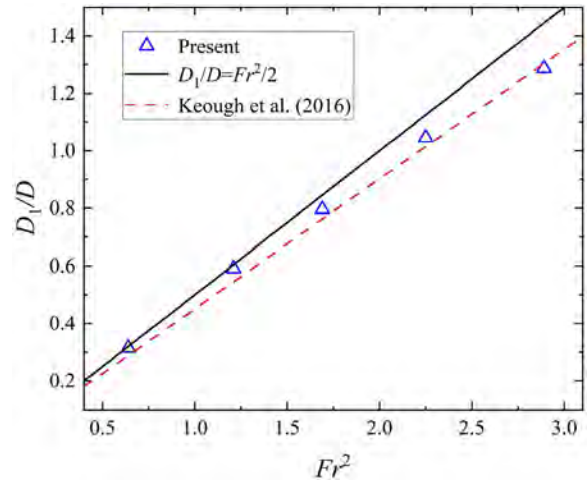


FIG. 8. Nondimensional bow wave height D_1/D at different Froude numbers.

computational mesh near the free surface at $t = 3$ s and $Fr = 1.3$. The mesh is very fine in the bow wave and wake region where the flow characteristics are complicated and coarse in the non-critical region.

C. Numerical validation

In this subsection, the global drag coefficients, bow wave height at various Froude numbers, and the free surface deformation at $Fr = 1.1$ are adopted to validate the present numerical approach.

Figure 7 compares the drag coefficients C_d of the cylinder at different Froude numbers with results from Ageorges *et al.*²⁰ In the study, C_d is calculated using: $C_d = F_d / (0.5\rho D h V^2)$, where F_d is the drag force. The calculated C_d decreases from 0.87 at $Fr = 1.1$ to 0.73 at $Fr = 1.7$, which conforms better to experimental results than previous LES results. The bow wave heights at different Froude numbers are plotted in Fig. 8. At lower Froude numbers, the values of the bow wave height conform to standard Bernoulli theory results. When the Froude number gets larger, the bow wave heights come near the modified

TABLE IV. Quantitative error analysis of the drag coefficient C_D and the bow wave height D_1/D .

Parameter	$Fr = 1.1$	$Fr = 1.3$	$Fr = 1.5$	$Fr = 1.7$	Average error
C_D	1.98%	1.11%	3.77%	0.68%	1.89%
D_1/D	8.38%	4.40%	3.05%	1.31%	4.28%

equation provided by Keough *et al.*¹⁷ Table IV provides the quantitative error analysis of the drag coefficient and the bow wave height. In summary, the bow wave height measurement accords well with theoretical and experimental results.

Figure 9 further plotted was the free surface deformation at $z/D = 0$ and $z/D = 1$ at $Fr = 1.1$. The trend of the free surface deformation corresponds well with the former experimental and numerical results, especially in front of the cylinder. However, the free surface

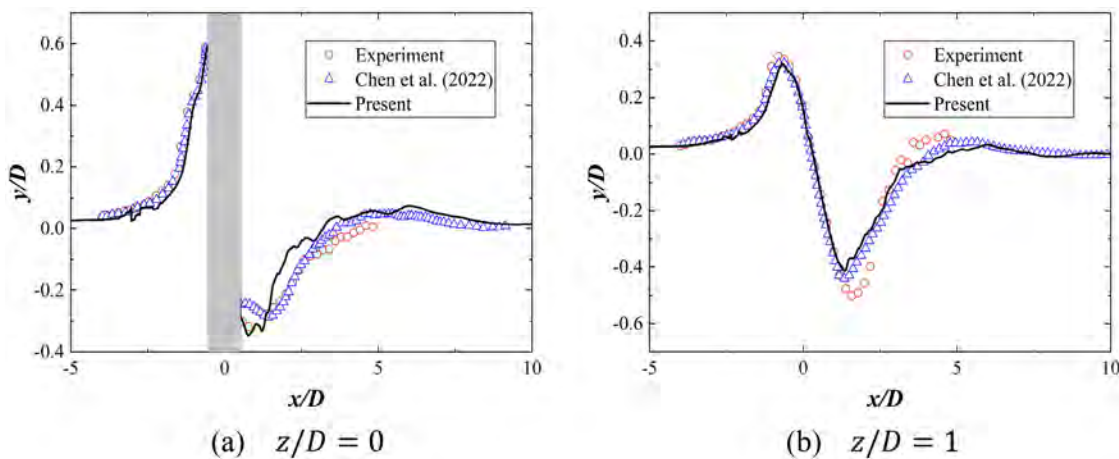


FIG. 9. Free surface deformation at $z/D = 0$ and $z/D = 1$ at $Fr = 1.1$.

deformation behind the cylinder slightly varies from the references. This is largely due to a different cylinder diameter and the ratio of draught and diameter chosen in this study. The ratio $h/D = 2.55$ is smaller than $h/D = 4$ in Ref. 26, resulting in a stronger free-end effect on the free surface which will be discussed in Sec. IV.

IV. FLOW CHARACTERISTICS

A. Surface deformation

The flow field at high Froude numbers varies greatly from that at lower Froude numbers. At the lower Froude number [$Fr = 0.8$, Fig. 10(a)], the change of the free surface is gentle with relatively small amplitudes of the crest and trough. The concave free surface behind the cylinder (or called the depression region) appears to be the fan shape with a few discontinuous points where air entrainment occurs. The wake area presents a continuous Kelvin waveform. As the Froude number increases to $Fr = 1.1$ [Fig. 10(b)], a spilling breaker forms before the cylinder. The trough of the free surface moves from the center to the two sides, making the depression region a “Wing” shape. The Kelvin waveform still exists, but the Kelvin wave crest moves far from the cylinder. A wave crest begins to form at the center behind the cylinder. At higher Froude numbers [$Fr = 1.3, 1.5, 1.7$, Figs. 10(c)–10(e)], the bow wave steepness in front of the cylinder continues to increase. The spilling breaker turns into plunging breaking bow waves with air entrainment and droplet splashing. The trough behind the cylinder turns into a “Y” shape. With the increase in the Froude number, the included angle of the top two branches of the “Y” or the wake angle decreases and the vertical stem of the “Y” becomes longer, conforming to former experimental and numerical results.^{14,20} The Kelvin waveform fully transforms into Mach-like wakes described by Rabaud and Moisy.^{40,41}

Strong wave breaking phenomena are observed for high Froude number cases. The wave breaking onset is the first step in fully understanding the wave breaking phenomenon.⁴² For two-dimensional Stokes wave breaking, Deike⁴³ provided a critical wave steepness $\epsilon = a_0 k = 0.32$ at high Bond numbers, where a_0 was the initial wave amplitude and k was the wave number. McAllister *et al.*⁴² recently presented an experimental study on a three-dimensional wave breaking. Three different wave breaking regimes were identified: (i) “traveling-wave breaking,” (ii) “standing-wave breaking,” and (iii) “traveling-standing-wave breaking.” It was found that the steepest non-breaking local surface slope $|\nabla\eta|$ reached over 0.8 in standing waves, much higher than the two-dimensional waves. In this study, we adopt the previous results and analyze the wave breaking in the flow past a surface-piercing circular cylinder. The local surface slope $|\nabla\eta|$ is defined as

$$|\nabla\eta| = \sqrt{\left(\frac{\partial\eta}{\partial x}\right)^2 + \left(\frac{\partial\eta}{\partial y}\right)^2}. \quad (9)$$

Note that the mesh resolution is different across the computational domain because of the adoption of the AMR technique. Therefore, the simulation results require resampling before calculating the local surface slope. To make sure an appropriate resampling mesh resolution ($\Delta x/D$) is chosen for the local surface slope calculation and the results are independent of the resolution, a sensitivity analysis is conducted at first. The variations of the two different indexes are chosen to measure the sensitivity: (i) the average local surface slope

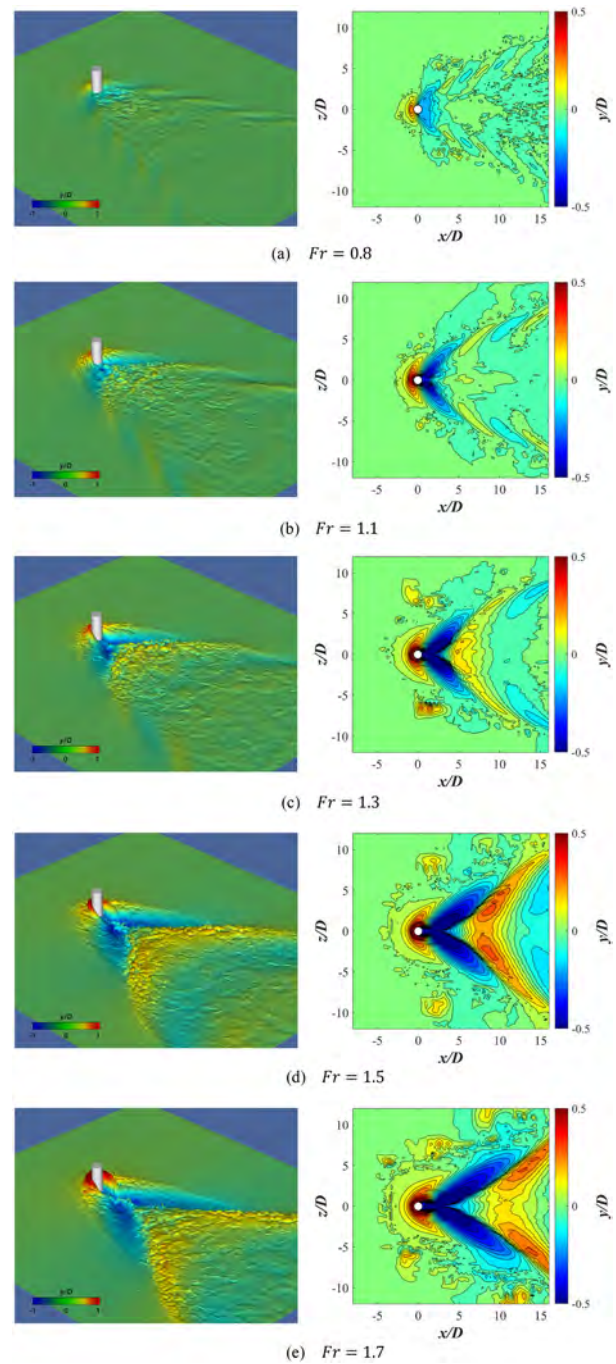


FIG. 10. Instantaneous free surface and time-averaged surface-elevation contour lines at various Froude numbers.

($|\nabla\bar{\eta}|$) and (ii) the area of $|\nabla\eta| > 1$ ($S_{|\nabla\eta|>1}$), which reflects the capture ability of the concerned region. The baseline mesh resolution is $\Delta x/D = 1/20$ and the results are shown in Fig. 11. When the mesh resolution varies by $\pm 20\%$, the errors in both indexes are within 5%. This indicates that the local gradient has a low sensitivity to the mesh

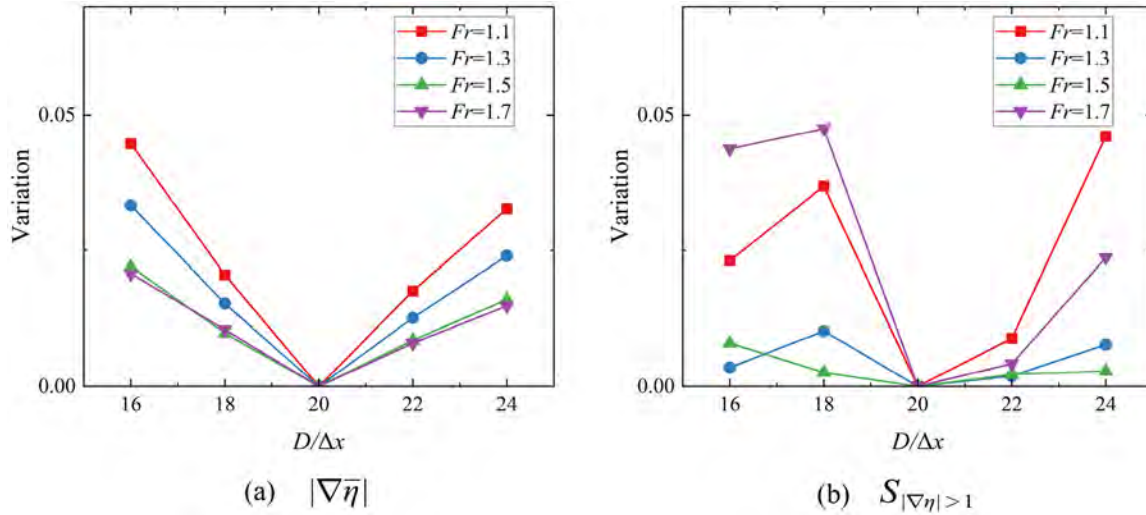


FIG. 11. Variations of the mesh resolution change on the local surface slope results.

resolution used for calculating the local surface slope. Therefore, using the resampling mesh resolution ($\Delta x/D = 1/20$) for data processing and analysis is appropriate.

Having determined the mesh resolution for the local surface slope analysis, Fig. 12 shows the local surface slope distribution at different Froude numbers. The regions where local surface slopes under 0.3 are filtered. Three high local surface slope regions are identified: (i) the bow wave region, (ii) the depression region, and (iii) the wake region. At $Fr = 1.1$, the “V-shaped” wake region is not confectioned, while at $Fr = 1.3$ and above, the wake region is complete with a decreasing angle and an increasing side length. Moreover, the high local surface slope wake regions identified in Fig. 12 fit well with the breaking region seen in the instantaneous free surface in Fig. 10. It proves that the local surface slope is a valid criterion for identifying wave breaking. Kelvin- or Mach-like wakes arising from the surface-piercing cylinder flow match the “traveling wave” described by McAllister *et al.*⁴² It is also observed that the high local surface slope region in the wake at $Fr = 1.3$ is not as widely distributed as that at $Fr = 1.5, 1.7$, but the width of the region and the peak slope area are larger. From Fig. 10, non-breaking waves with steep local slopes are observed at the side of the cylinder. These two waves meet at the depression region behind the cylinder and form vertical jets at high Froude numbers. The phenomenon matches the “standing-wave breaking” regime, where the slope of wave breaking onset is much higher than “traveling-wave breaking.”

B. Characteristics of the velocity field

In this subsection, we mainly discuss the flow characteristics related to the velocity field. We start by plotting the non-dimensional average velocity distribution on certain locations in the velocity fields. As shown in Fig. 13, three specific locations on the streamwise ($x/D = -1, 1, 2$) and vertical directions ($y/D = -0.5, -1.5, -2.5$) are chosen, respectively, making nine concerned cross-stream lines (L1~L9). For the streamwise or horizontal direction, $x/D = -1$ represents the location in front of the circular cylinder, $x/D = 1$ represents the location near the back of the circular cylinder, and $x/D = 1$

represents the location farther behind the circular cylinder. For the vertical direction, $y/D = -0.5$ represents the location near the interface, which is more influenced by the free surface, $y/D = -1.5$ represents the location at the middle of the immersed part, which is closer to the single-phase condition, and $y/D = -2.5$ represents the location near the free end, where free end effects are more considered.

Figure 14 shows the streamwise velocity distribution. The streamwise velocity shows a consistent pattern across different Froude numbers in front of the circular cylinder (L1, L4, and L7). It reaches a minimum value at the center of the x - y plane and increases rapidly toward the cross-stream direction. The minimum values of the streamwise velocity in front of the cylinder are slightly different near the free surface. However, at $Fr = 1.5, 1.7$, the minimum values near the free end vary from lower Froude number cases with two symmetry locations, indicating distinct flow regimes at the free end. The streamwise velocity also shows a consistent pattern behind the cylinder at $y/D = -1.5$. The deformation of the free surface contributes to the velocity change near the free surface. However, the maximum value of the streamwise velocity decreases and the maximum velocity point is closer to the center with the increase in the Froude number, indicating the regime transition of the free surface deformation and reduced separation area at higher Froude numbers. This observation is distinct from the variation trend of the separation area with the Froude number at $Fr < 1$ recorded by Suh,²³ suggesting that the trend of separation near the free surface varies with the Froude number range. For higher Froude numbers ($Fr > 1$), the velocity pattern conforms to the Kelvin- and “Mach-like” wake transition pattern discussed above. The streamwise velocity reduced more intensely near the free end at $Fr = 1.5, 1.7$ behind the cylinder (L8, L9). It also influences the streamwise velocity further behind the cylinder (L6).

Figure 15 shows the vertical velocity distribution. Near the free surface, the vertical velocity near the front of the cylinder (L1) shows an upward trend. This indicates that the flow is being lifted due to the presence of the cylinder, which disrupts the flow and creates a region of low pressure in front of it. At $Fr = 0.8$, the vertical velocity near the

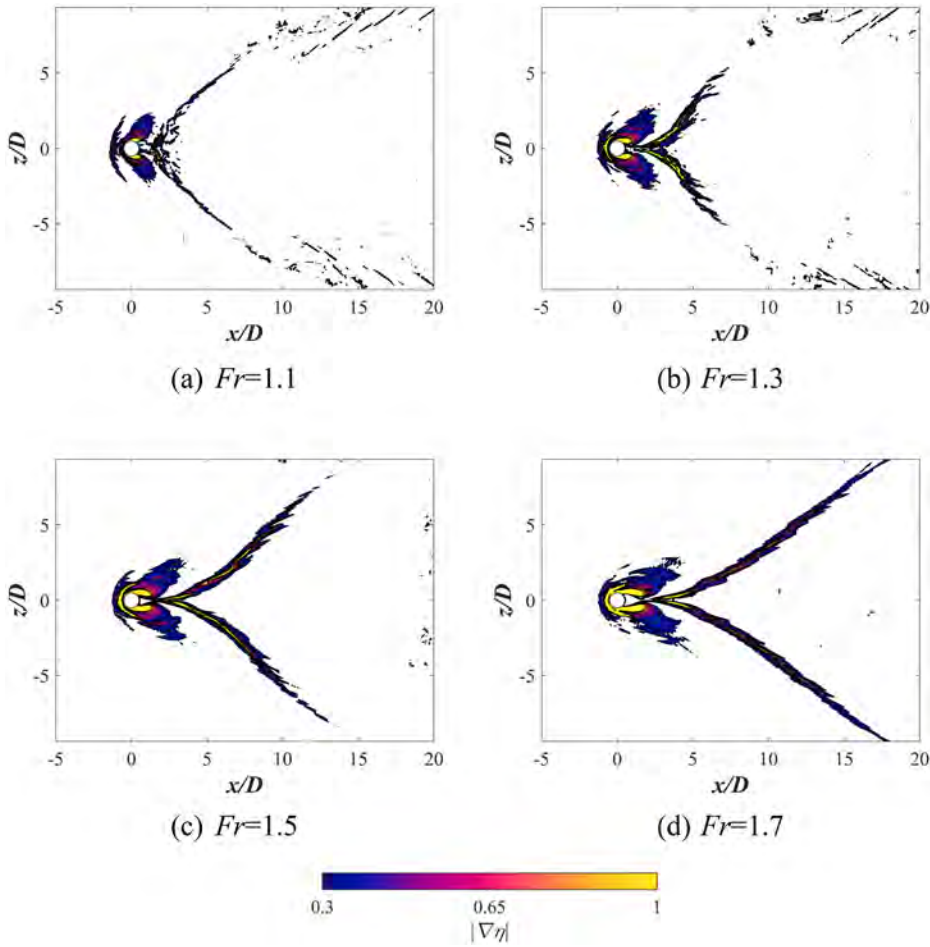


FIG. 12. Local surface slope $|\nabla\eta|$ of the average wave height.

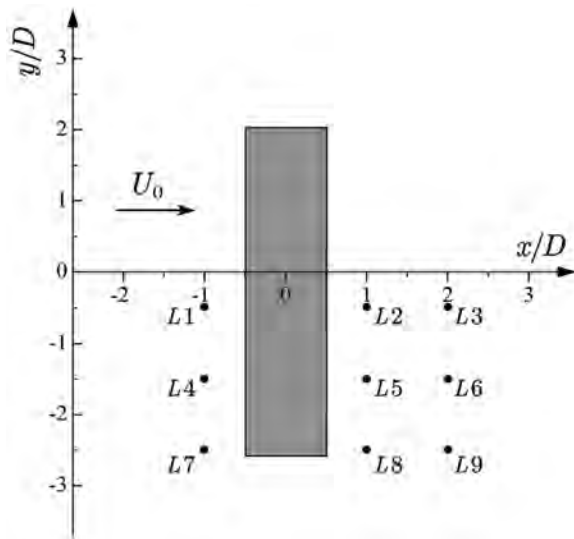


FIG. 13. The concerned locations of the velocity field.

free surface shows an opposite direction compared to higher Froude numbers. This corresponds to different bow wave forms, such as continuous, spilling, and plunging. The vertical velocity near the free surface behind the cylinder is complicated, but a “W-shaped” velocity distribution is observed at all Froude numbers. At $Fr = 1.1$, there is a peak of the vertical velocity at the centerline at L2. Similar observations at P5 and P8 imply a unique upward flow regime at this critical Froude number. The vertical velocity near the free end behind the cylinder takes on a pulse shape (L8, L9). The free-end effect and a strong upward flow behind the cylinder suppress the flow separation. The maximum values of the vertical velocity near the free end at $x/D = 1$ for $Fr = 1.3$ and below are larger, while at $x/D = 2$, the maximum values for $Fr = 1.5, 1.7$ are larger. This suggests that the upward flow behind the cylinder is delayed at higher Froude numbers.

Figure 16 shows the cross-stream velocity distribution. The cross-stream velocity in front of the cylinder shows a consistent pattern at different Froude numbers like the streamwise and vertical velocity. As the Froude number increases, the maximum value of the cross-stream velocity slightly decreases in the middle and near the free surface. Near the free end, the peak of the cross-stream velocity is significantly reduced. However, the free end contributes to the outward flow behind the cylinder, making the peak much larger than that in the middle.

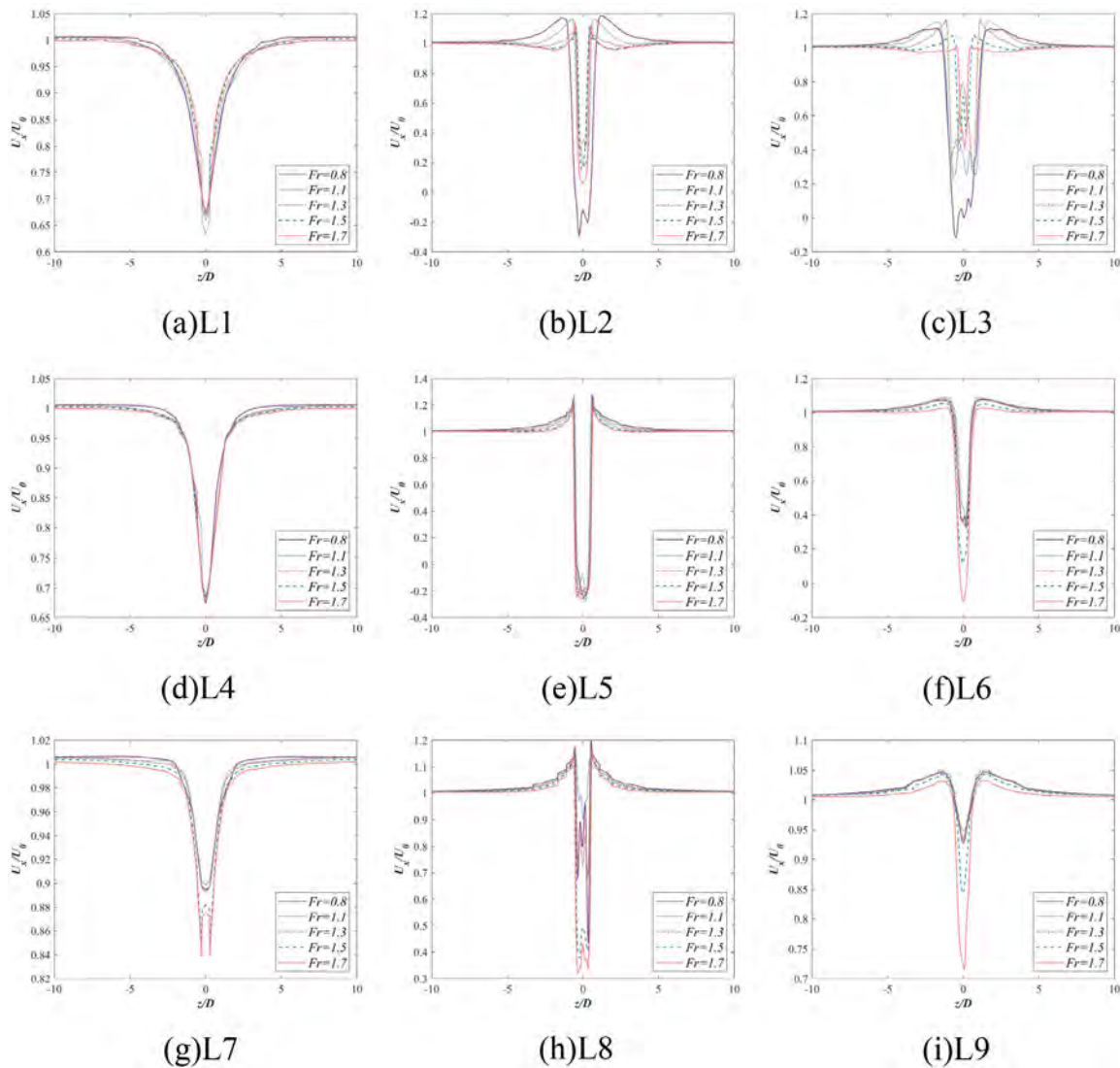


FIG. 14. Time-averaged lines for the streamwise component of velocity.

The free surface provides a similar contribution. At higher Froude numbers, the maximum value of the cross-stream velocity at $x/D = 2$ are larger than those at $x/D = 1$. This observation corresponds to other velocity components and accounts for the longer depression region at higher Froude numbers. The cross-stream velocity near the free end behind the cylinder is also affected by the upward flow. The peak cross-stream velocity near the free end at $x/D = 1$ for $Fr = 1.1$ is more significant but at $x/D = 2$ the peak cross-stream velocity for $Fr = 1.7$. It is consistent with the vertical component and suggests that the upward flow suppresses the flow separation.

To further visualize the free surface and free end effect on the cylinder flow, the time-averaged velocity distributions at $z/D = 0$ are shown in Fig. 17. Note that the arrows in Fig. 17 only represent the direction of the local velocity rather than the magnitude, some arrows penetrate the cylinder, but the velocity at the cylinder surface is zero

according to the colormap. Several typical features are observed. In the bow wave region, a velocity reduction is found under the bow wave in the water phase and along the bow wave crest in the air phase, proving the reasonability of the Bernoulli equation in bow wave height prediction. Flow separation is observed at the free end in the water and air. With the increase in the Froude number, the low-speed region behind the cylinder in the water phase grows larger. Backward flow is observed and a vortex is formed near the free end at high Froude numbers. At $Fr = 1.3$ and above, a high-speed region under the free surface and a low-speed region above is observed. The region's area also grows larger with the increase in the Froude number, indicating stronger shear near the free surface.

The non-dimensional turbulent kinetic energy TKE is adopted to visualize the fluctuation of the velocity field at the free surface in Fig. 18. In this study, the value of TKE is calculated as follows:

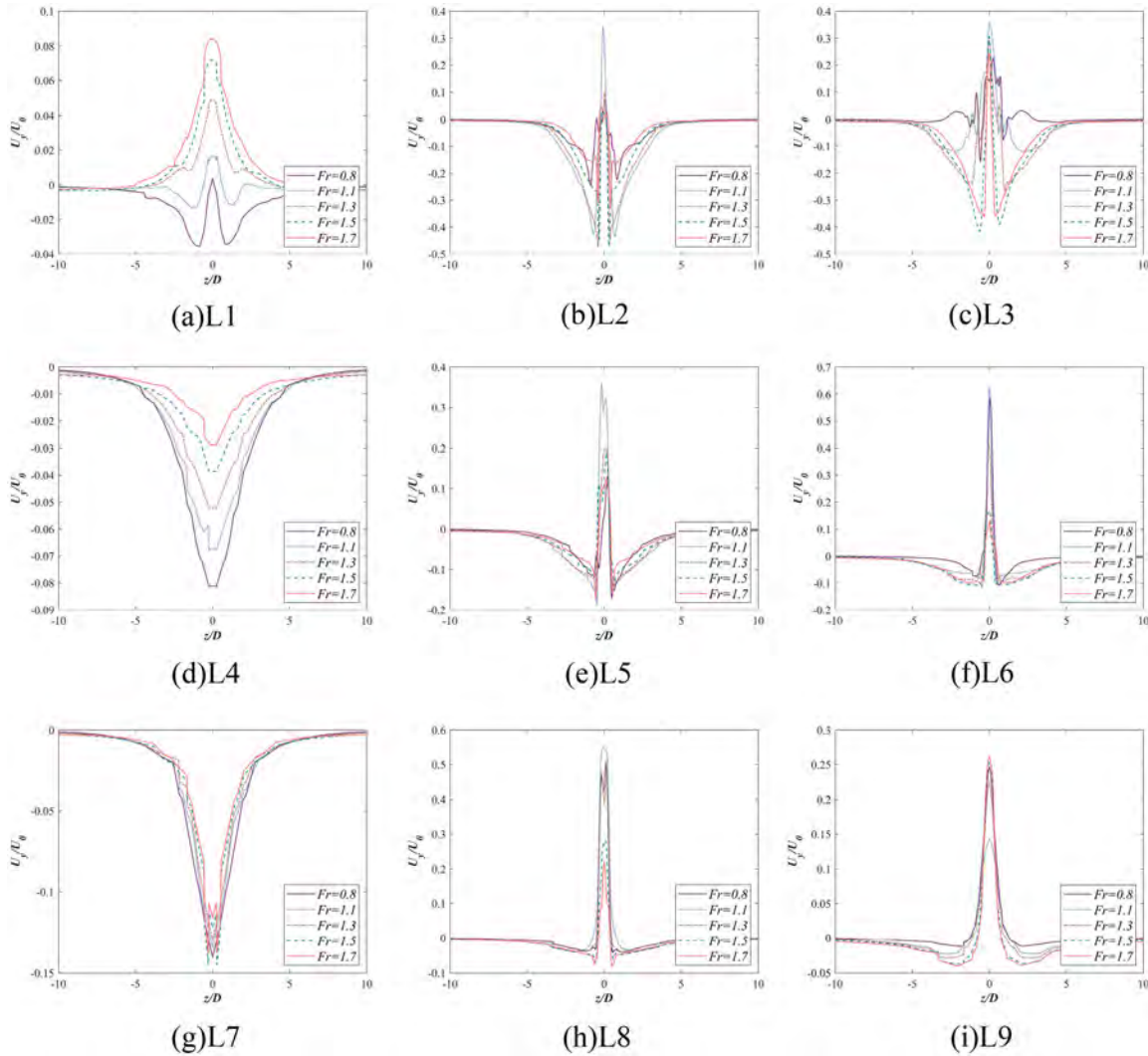


FIG. 15. Time-averaged lines for the vertical component of velocity.

$$TKE = \frac{1}{2} (u_x'^2 + u_y'^2 + u_z'^2) / U_0^2, \quad (10)$$

where $u' = u - \bar{u}$ is the instantaneous velocity fluctuation. The turbulent kinetic energy at the free surface is mainly distributed in the bow wave region and the wake region where wave breaking occurs as mentioned in Sec. IV A. Several turbulent kinetic energy peaks are observed, corresponding to the instantaneous bubble and droplet formation process. At $Fr = 1.7$, a large area of high turbulent intensity is observed in front of the circular cylinder, suggesting that strong plunging wave breaking occurs in this region. In the spilling breaking cases where air entrainment is limited, the turbulent intensity is reduced a lot. In the wake region, the turbulent kinetic energy occupies quite a large “fan-shaped” area at $Fr = 1.1, 1.3$, which is also observed in the former study.²⁶ However, at higher Froude numbers a different distribution is observed. The peaks of the turbulent kinetic energy are dispersed along the two “Mach-like” wave crests. The turbulent intensity

near the back of the cylinder reduces, with two symmetry laminar regions appearing between the bow wave and the “Mach-like” wake.

C. Vortex structures

Three-dimensional instantaneous vortex structures extracted using Q -criterion contour⁴⁴ $Q = 520$ at different Froude numbers with a side view and an upward view are shown in Fig. 19. The vortex structures are colored by the magnitude of the vorticity. Near the free surface, the vortex structures are mainly composed of small-scale structures due to the free surface deformation. Large vortex structures are observed to detach from the surface of the middle cylinder, which are known as the Karman vortex shedding. The structures near the free end show an upward-sloping trend, which corresponds well to the measurement of the velocity distribution and observation in the previous study by Chen *et al.*²⁶ It is observed that the wake structures at the free end show distinct characteristics at different Froude numbers. At

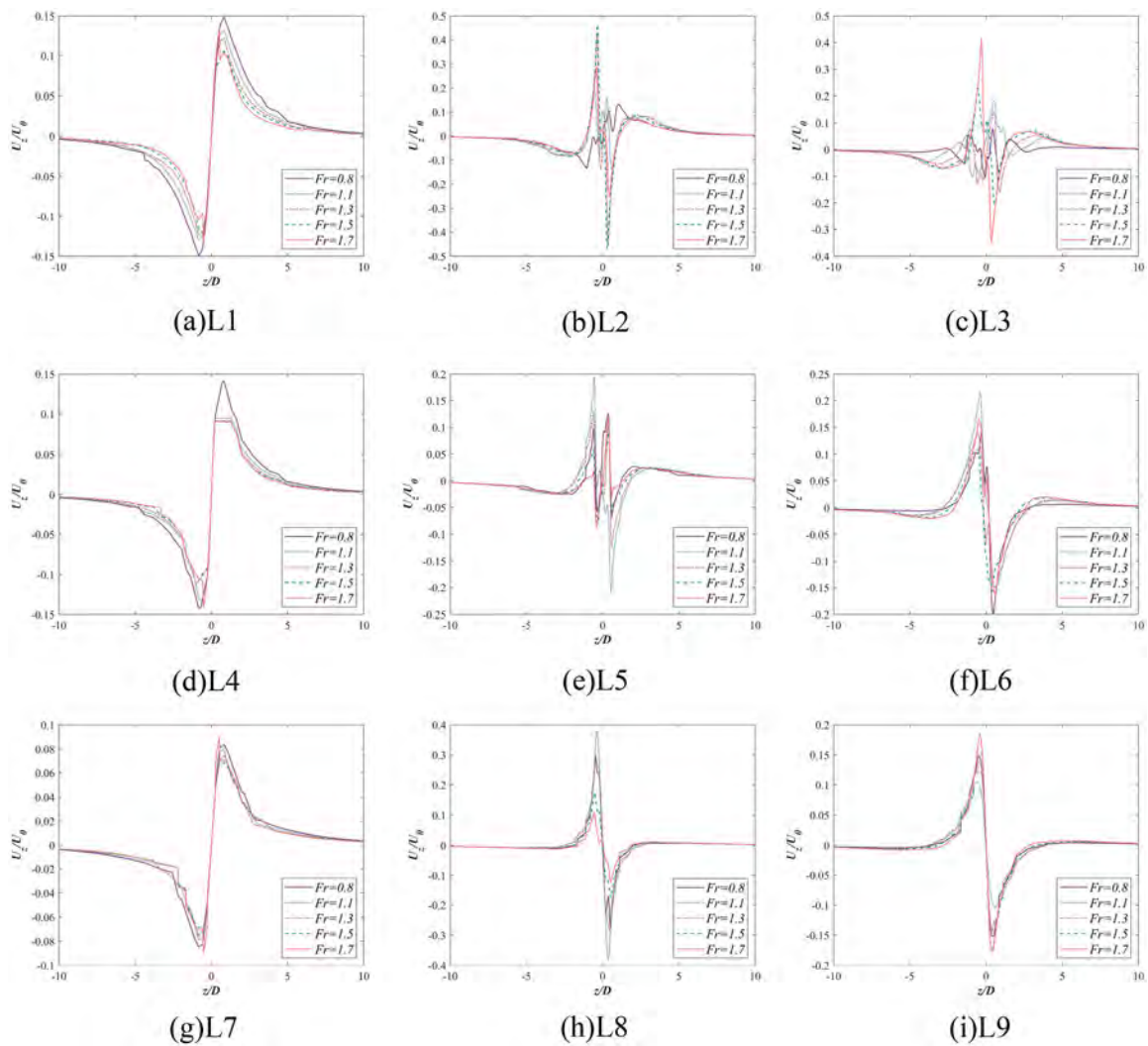


FIG. 16. Time-averaged lines for the cross-stream component of velocity.

$Fr = 0.8$, the structures at the free end quickly join into the primary vortex in the middle and have little influence on the subsequent development, suggesting that the free end effect is insignificant at low Froude numbers. The slope of the upward trend at the free end reaches a maximum value at $Fr = 1.1$ and decreases with the increasing Froude number. It indicates that at medium and high Froude numbers, the free end effect is more crucial; however, it is delayed and reduced by a stronger inlet velocity. From the upward view, distinct characteristics are also observed at different Froude numbers. The vortex structures only distribute behind the circular cylinder at $Fr = 0.8$, with the Kelvin wave region remaining laminar flow. At higher Froude numbers especially at $Fr = 1.5, 1.7$, the vortex structures also appear in the breaking wake on both sides. The observation suggests that wake turbulence from the surface-piercing cylinder has two main components: (i) the vortex structures detached from the cylinder surface and (ii) the vortex structures generated by the breaking wake.

To further quantify the three-dimensional features of the vortex structures, Fig. 20 plots the areas of the vortex region ($Q > 520$) at different vertical locations. The area of the vortex region S_Q is non-dimensional by the cylinder diameter D . It is observed that for all Froude numbers, the areas of the vortex show a growing trend from the free end to the free surface. This conforms to the observation of the upwash flow. The stronger upwash flow at $Fr = 1.1, 1.3$ is also quantified by the increasing speeds of the vortex region area match a quadratic power law. On the contrary, the increasing speeds of the vortex region area match a linear power law at other Froude numbers. The vortex region area of $Fr = 0.8$ at the free surface is much smaller than other Froude numbers, demonstrating that the vortex structures near the free surface is generated by the wave breaking.

Figure 21 shows the local vortex structures near the cylinder and beneath the breaking wake to provide a deeper insight into the components of the vortex structures. In Fig. 21(a), the vortexes

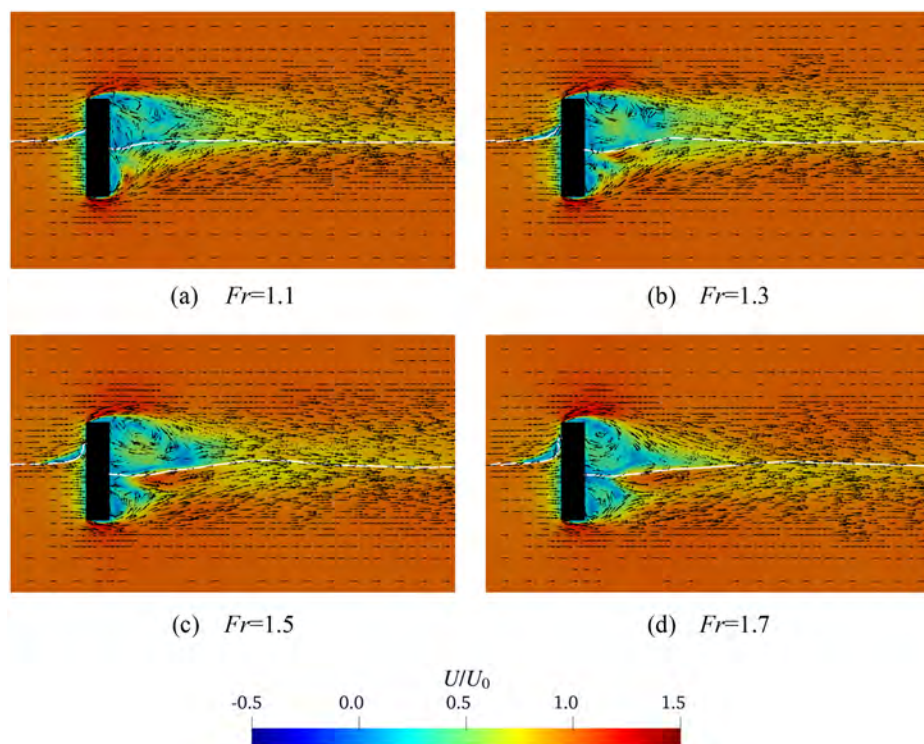


FIG. 17. Time-averaged velocity distribution at $z/D = 0$ (white line: free surface).

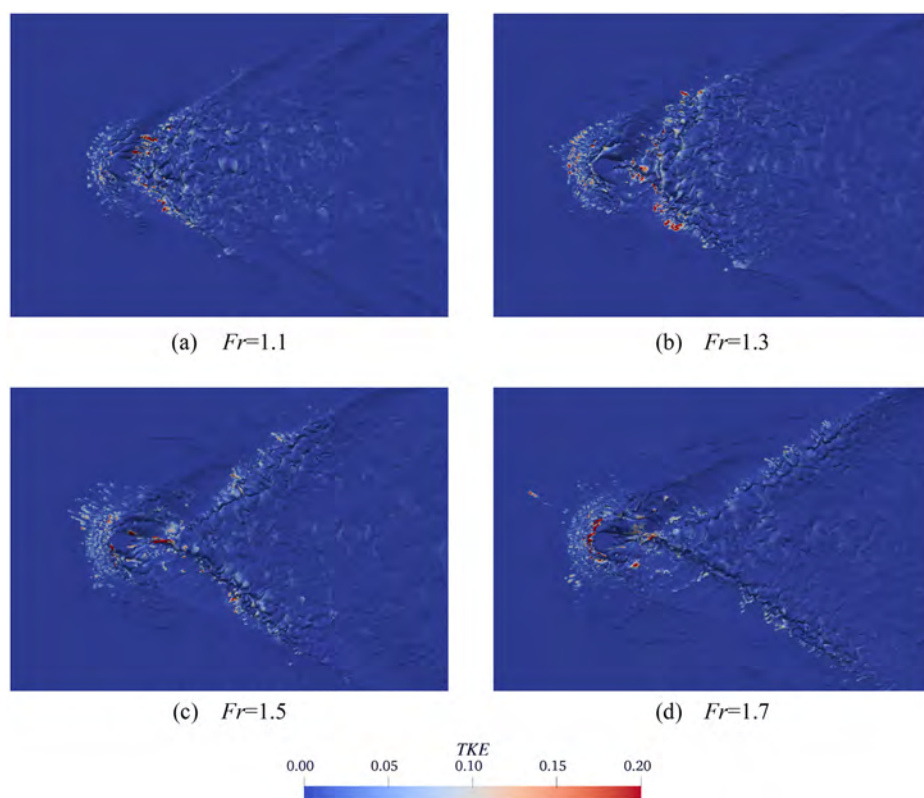


FIG. 18. Contours of turbulent kinetic energy at different Froude numbers.

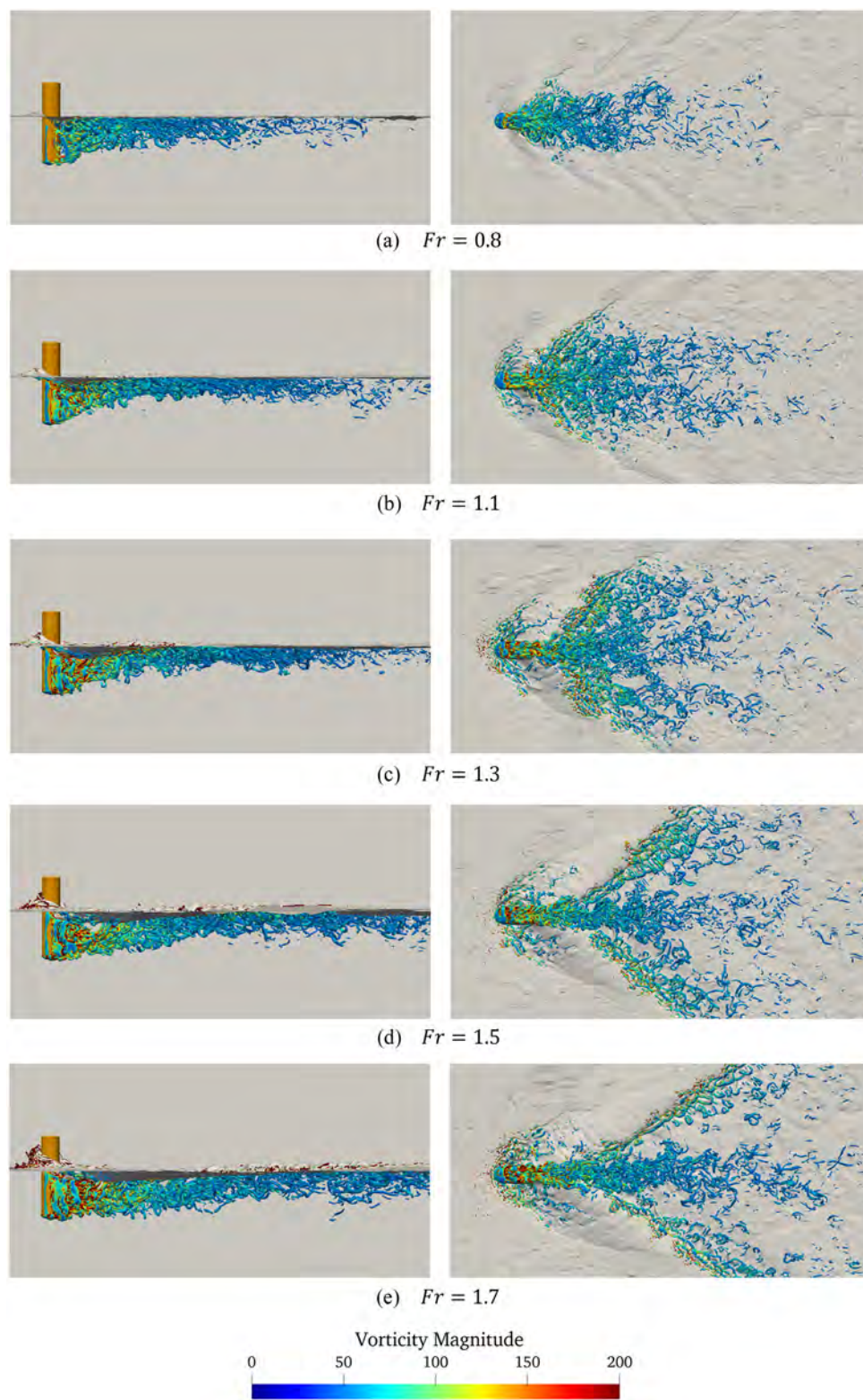


FIG. 19. Global view of the vortex structures at different Froude numbers.

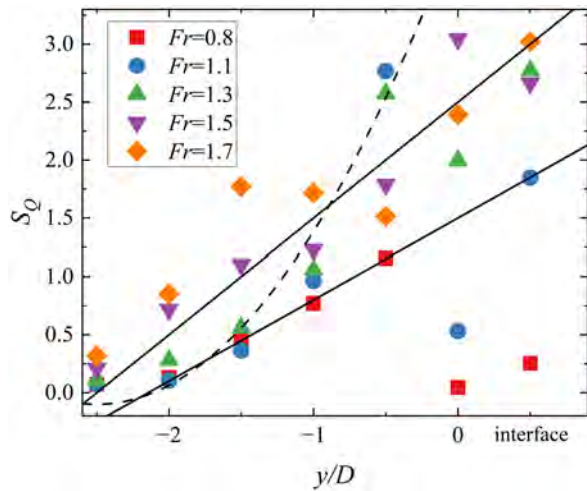


FIG. 20. Areas of the vortex region at different vertical locations (solid line: linear; dashed line: quadratic).

induced by air entrainment are distributed in the depression region. In addition to these vortices, there are no other vortex structures in this region. Necklace vortices surrounding the front of the cylinder are also observed. They form from the coming flow and the reverse flow near the front stagnation point.²⁶ It is also observed that the necklace vortices on the side are connected to the air entrainment induced vortices by streamwise vortex filaments. The necklace vortices near the free surface contribute to free surface breaking and act as the source of the air entrainment induced vortices, revealing the close relationship between the two types of vortices. The streamwise vortex filaments are observed in Fig. 21(b), which make up the main vortex structures in the breaking wake. Similar vortex structures are observed in the study of Stokes breaking wave.^{45,46} Together with the observations in the free surface deformation, it suggests that the breaking wake and the Stokes breaking waves belong to the same category of wave breaking.

V. AIR ENTRAINMENT AND BUBBLE STATISTICS

In this section, we dive into the air entrainment and bubble statistics in the flow past a surface-piercing circular cylinder at high Froude

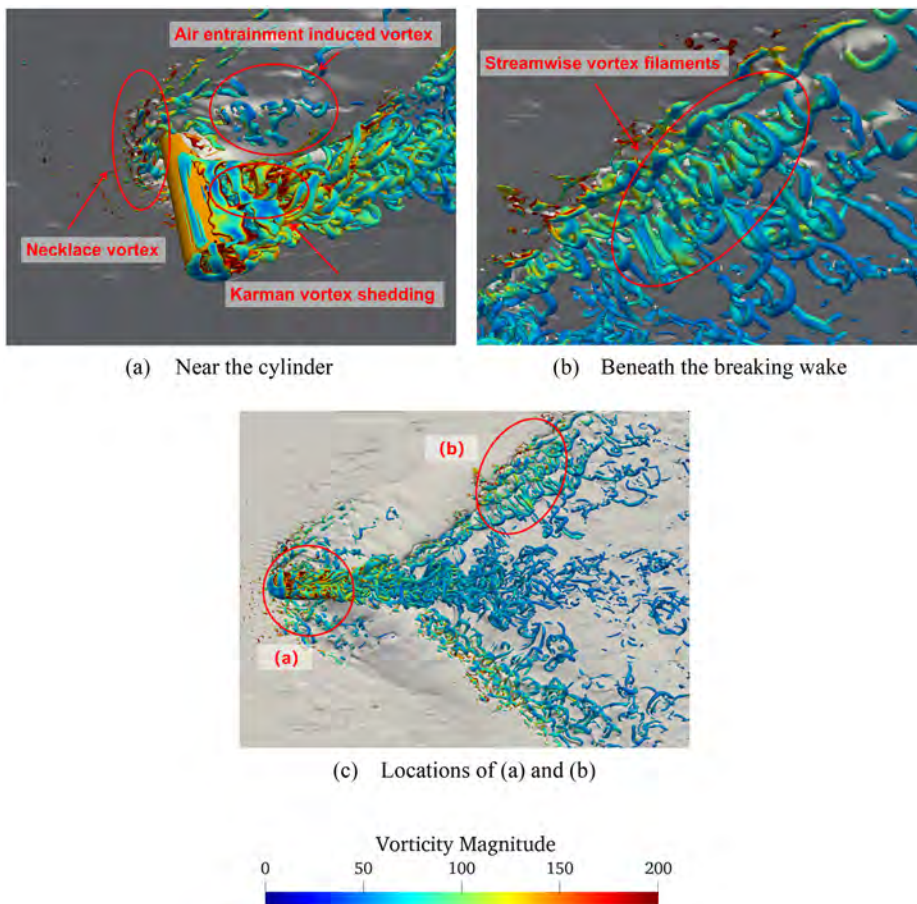


FIG. 21. Local vortex structures at $Fr = 1.5$.

22 March 2025 20:10:18

numbers. The locations and the volumes of the bubbles are counted using the technique mentioned in Deike *et al.*⁴⁷ We focus especially on the close relationships between bubble statistics and the flow field characteristics discussed in Sec. IV.

A. Bubble size distribution

The size distribution of bubbles is a widely used approach to characterize the bubble dynamics.^{47–50} Figure 22 shows the time-averaged bubble size distribution. N_r represents the number of bubbles distributed by bubble radius. The number of bubbles smaller than 2 mm is similar at different Froude numbers, while the number of larger bubbles at $Fr = 1.1$ is less than that at higher Froude numbers. However, there was no significant difference in bubble size distribution at $Fr = 1.3, 1.5,$ and 1.7 . One possible reason for this phenomenon is that the bubbles are counted in the entire computational domain. At $Fr = 1.5, 1.7,$ the breaking wake is much closer to the outlet, leading to a decrease in the number of bubbles remaining in the computational domain. Three different slopes of bubble size distribution are observed. The first and second slope is $N_r \sim r^{-3/2}$ and $N_r \sim r^{-10/3}$, which is widely observed in the studies of breaking waves.^{47,49,51} These two slopes correspond to bubbles whose radius is under 3 mm and are mainly distributed in the fully developed wave breaking region. For larger bubbles and cavities, a third slope which is much steeper is observed in this study. Figure 23 plots the bubble size distribution over time at $Fr = 1.3$ and provides a deeper insight into the phenomenon. N_r represents the number of bubbles distributed by time. It is observed that the number of bubbles whose radius is smaller than 3 mm is stable over time, suggesting that the formation and bursting of bubbles are in dynamic equilibrium at this scale. On the contrary, rapid fluctuations in quantity over time can be observed for large bubbles. It suggests that the formation frequency of large bubbles is lower than the fragmentation frequency. Therefore, they are at the top of the cascade of bubble fragmentation events and closely related to the air entrainment onset.

B. Bubble spatial distribution

First, the numerical results of the bubble spatial distribution at $Fr = 1.3$ are compared to the experimental photograph from

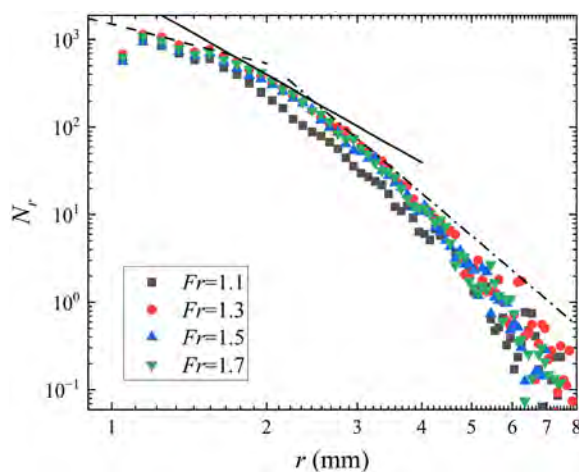


FIG. 22. Time-averaged bubble size distribution at different Froude numbers (dashed line: $N_r \sim r^{-3/2}$; solid line: $N_r \sim r^{-10/3}$; and dot-dashed line: $N_r \sim r^{-5}$).

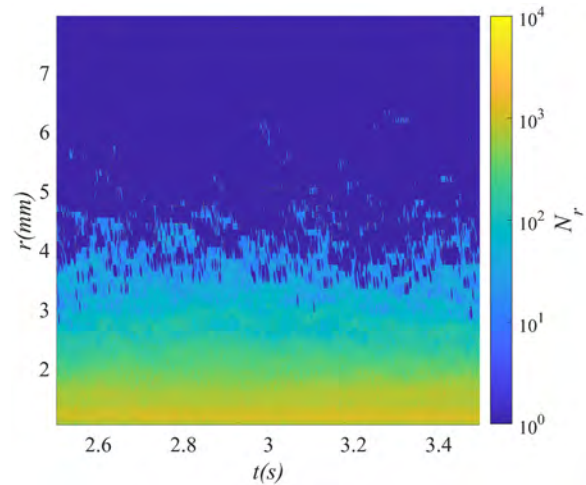


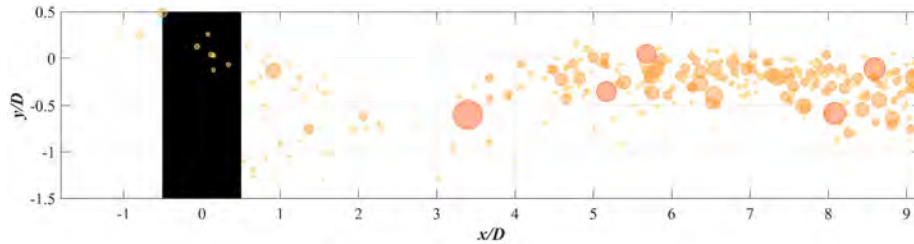
FIG. 23. Bubble size distribution over time at $Fr = 1.3$.

Ageorges *et al.*¹⁹ in Fig. 24. It is observed that the spatial distribution of bubbles is well captured in the numerical results, corresponding to three air entrainments from the three wave breaking regions. A slight difference is observed that the rising area of the bubbles entrained in the bow wave and depression region in the numerical simulations is at $3 < x/D < 4$, which is ahead of the area observed in the experiment. A possible reason for the phenomenon is that the draught-diameter ratio of the cylinder h/D is smaller than that in the experiment. Figure 25 shows the vortex structures of two different draught-diameter ratio cylinders. It is observed that the upwash flow generated from the free end has an impact length of about $1.5D$ vertically, and the vertical distribution range of the bubble is $-1.5 < y/D < 0$ at $Fr = 1.3$, which explains that if the draught-diameter ratio of the cylinder is smaller than 3, the upwash flow will influence the bubble spatial distribution by accelerating the rise of bubbles.

Figure 26 shows the instantaneous spatial distributions of bubbles at different Froude numbers. Sub-figures on the left show the spatial distribution in the x - y plane, and sub-figures on the right show the spatial distribution in the x - z plane. At $Fr = 1.1$, the bubbles are mainly distributed in the vertical region between $y/D = 0$ and $y/D = -1$. The deepest bubble reaches $y/D = -1.56$. Large cavities are formed in the wake behind the cylinder, split into small clusters of bubbles in cascades, and move with the wake. At $Fr = 1.3$, more bubbles are observed at the back of the cylinder, but the number of bubbles in the depression region is still limited. This observation is consistent with the observation in the local surface slope (Fig. 12), the turbulent kinetic energy (Fig. 18), and the vortex structures (Fig. 19). In the wake region, bubbles are more widely distributed in the vertical direction. Some bubbles are twisted into deeper areas at $x/D \approx 13$ and $x/D \approx 17$, corresponding to the characteristic of the plunging breaking wake. At $Fr = 1.5$ and $Fr = 1.7$, the deepest bubbles near the back of the cylinder reach the end of the finite cylinder, with a depth of $y/D = -2.59$. This observation conforms to the observation of the velocity field, where the upward flow is delayed (Fig. 15) and a strong vortex is formed near the free end behind the cylinder (Fig. 17) at higher Froude numbers. However, no bubbles are found deeper than the free end, and the upward movement of the bubbles is observed.



(a) Experiment photograph from Ageorges et al.¹⁹



(b) Numerical result in the present study

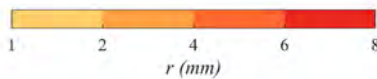


FIG. 24. Comparison of the vertical distribution of the bubbles at $Fr = 1.3$.

This is distinct from the experimental photographs recorded by Hilo *et al.*,²¹ in which the draught of the circular cylinder is much larger, suggesting the upward flow motivated by the free end greatly impacts the vertical spatial distribution of the bubbles. Moreover, large bubbles and cavities are observed to be dispersed along the wake crest, which conforms to the turbulent kinetic energy peak distribution (Fig. 18).

From the discussion of bubble size distribution, the locations of large bubbles and cavities strongly relate to the air entrainment onset. Figure 27 shows the density spatial distribution of bubbles whose radii are larger than 3 mm over time and further demonstrates the perspective. N_D represents the counted number of bubbles over a second in a certain area non-dimensioned by the cylinder diameter. It is observed that the regions where large bubbles and cavities are concentrated conform to the high local surface slope region. Three

air entrainment mechanisms are discovered: (i) by the breaking bow wave, (ii) by the breaking depression region, and (iii) by the breaking wake. Among the three mechanisms, the breaking wake contributes most of the bubbles. The number of large bubbles gradually decreases with the flow direction, making some streamwise lines. It suggests that larger bubbles and cavities are subjected to turbulent shearing effect when moving with the flow and eventually fragment into smaller bubbles. A relatively dispersed distribution of large bubbles and cavities in the wake region is observed at high Froude numbers, corresponding to the dispersed distribution of the peak of the turbulent kinetic energy. It indicates that turbulent kinetic energy peak is a characteristic of the air entrainment process on turbulent structures. Moreover, the streamwise bubble lines are longer at $Fr = 1.5, 1.7$, indicating that the large bubbles are longer-lived and subject to less turbulent shear. This can be proved by the vortex



(a) $h/D = 2.55$

(b) $h/D = 4$

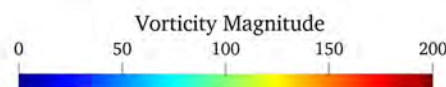


FIG. 25. Vortex structures near the cylinder of two draught-diameter ratios.

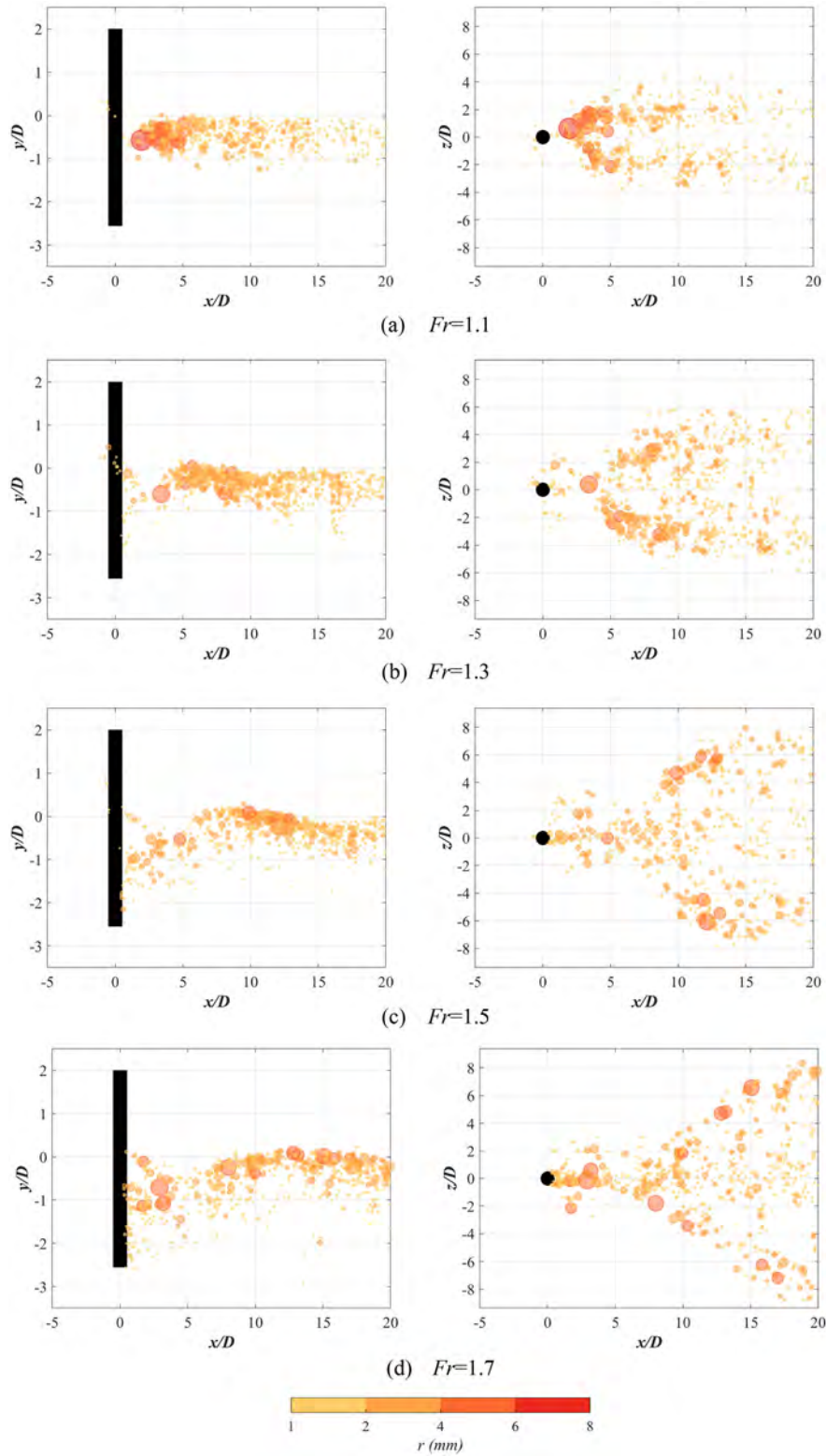


FIG. 26. Instantaneous spatial distribution of bubbles (left: x-y plane; right: x-z plane).

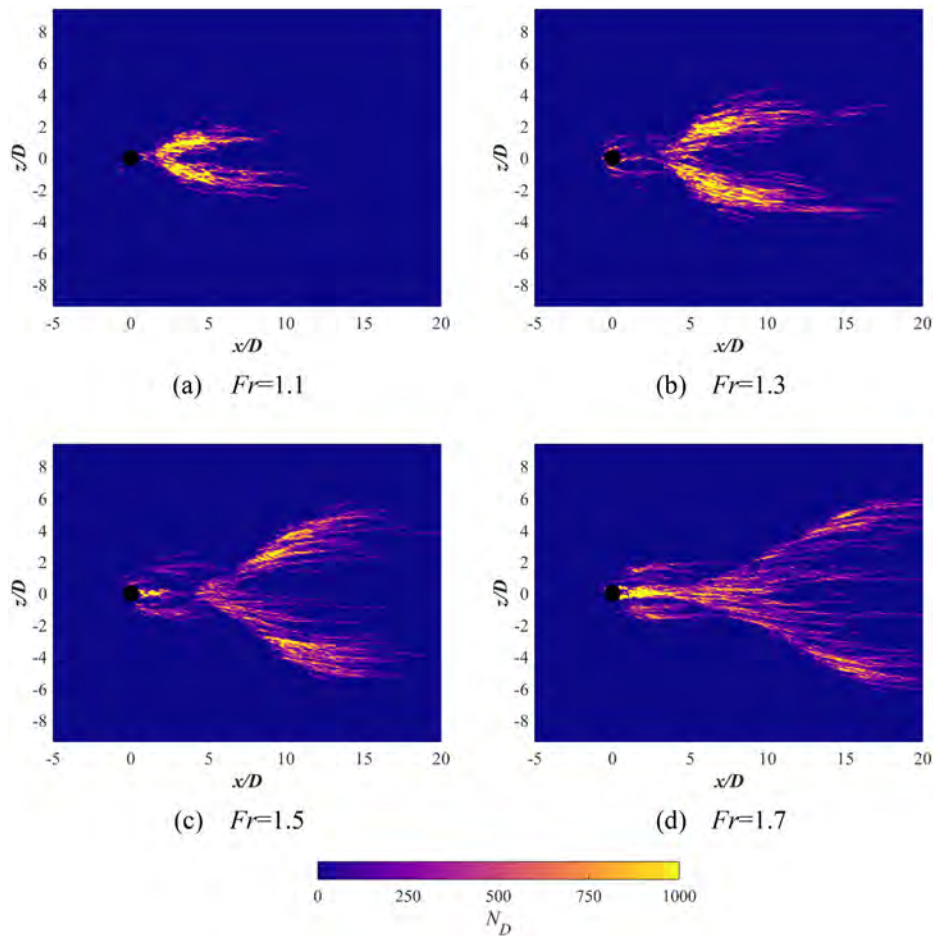


FIG. 27. Spatial distribution of bubble radius larger than 3 mm over time.

structures shown in Fig. 19, where sparser vortexes are observed behind the wake at higher Froude numbers.

C. Surface tension effects on bubble distribution

In previous studies on bubble statistics, many researchers have paid attention to the surface tension effects on the bubble distribution and dynamics.^{47,49,52,53} The surface tension effects on bubble distribution are discussed with the simulation result at $Fr = 1.3$ and four different Bond numbers classified into three categories: low ($Bo = 100$), medium ($Bo = 340, 1000$), and high ($Bo = 3400$).

Figure 28 shows the number of bubbles over time and the bubble size distributions for different Bond numbers. It is observed that the number of bubbles at the low Bond number is significantly less than that at medium and high Bond numbers. As shown in Fig. 29, a stronger surface tension effect results in the reduction of the wave breaking at the free surface, thus suppressing the air entrainment process. It is observed from the bubble size distribution that although the total bubble number is much lower, the power law discussed in Sec. VA is still suitable for describing the size distribution at the low Bond number. The number of bubbles at the high Bond number is larger than that at the medium Bond number. This phenomenon is mainly contributed by the bubbles with the lowest radius, which indicates that the surface

tension affects the break up speed of the bubbles, especially for the smaller bubbles. Figure 30 shows the side view of bubble spatial distribution at different Bond numbers to further uncover the surface tension effect on the bubble statistics. At $Bo = 100$, the bubble density is less than that at higher Bond numbers, but the spatial distribution is similar. With the increase in the Bond number, more large bubbles are observed in the flow field, mainly distributed near the free surface. It also illustrates that lower surface tension leads to more severe wave breaking and air entrainment. At $Bo = 3400$, large bubbles are hardly seen beneath $y/D = -0.5$, indicating that the bubble break up process is enhanced without the resistance of surface tension. In summary, the surface tension has a strong effect on the free surface breaking and the air entrainment process. However, the bubble spatial distribution has a closer relationship to the characteristics of the velocity field as discussed in Sec. VB.

VI. CONCLUSIONS

In this study, the flows past a surface-piercing circular cylinder at Froude numbers ranging from 0.8 to 1.7 are simulated using high-fidelity CFD tools. The flow and air entrainment features are analyzed thoroughly with the relationship between bubble statistics and flow field highlighted, providing new insights into the flow past a surface-

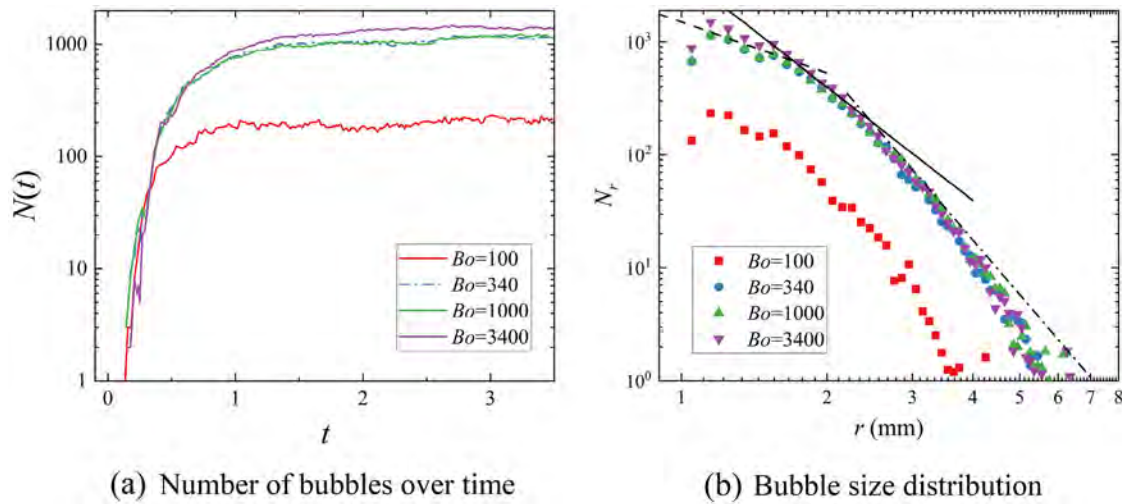


FIG. 28. Number of bubbles over time and bubble size distributions for different Bond numbers.

piercing circular cylinder at high Froude numbers. The main conclusions are as follows:

- (1) The free surface deformation at high Froude numbers varies greatly from that at lower Froude numbers. A “Mach-like” wake replaces the continuous Kelvin waveform and strong wave breaking is observed. By applying the local surface slope $|\nabla\eta|$ to the results, three distinct surface breaking regions are identified in the flow field: (i) the bow wave region, (ii) the depression region, and (iii) the wake region. The surface breakings in the bow wave region and the depression region correspond to the “standing-wave breaking” regime. In contrast, the surface breakings in the wake region match the “traveling-wave breaking” regime.
- (2) The velocity field exhibits many regular and distinctive characteristics at various Froude numbers. The free surface deformation contributes to the separation near the free surface. With the increase of the Froude number, the transition of the wake regime leads to a reduced separation area. In contrast to the free surface, the existence of the free end suppresses the flow separation, with a strong upward velocity observed behind the

cylinder near the free end. The peaks of turbulent kinetic energy are mainly distributed in the “fan-shaped” area at $Fr = 1.1, 1.3$ and dispersed along two “Mach-like” wave crests at $Fr = 1.5, 1.7$. Additionally, several typical vortex structures are captured using the Q -criterion, including necklace vortices, air entrainment induced vortices, streamwise vortex filaments, and the Kalman vortex shedding. The surface breaking and air entrainment are discovered as the origin of the streamwise vortex filaments in the wake region at high Froude numbers.

- (3) The air entrainment and bubble statistics in the cylinder flow are thoroughly investigated. Three different slopes—(i) $N_r \sim r^{-3/2}$ and (ii) $N_r \sim r^{-10/3}$ for small bubbles mainly distributed in the fully developed wave breaking region and (iii) $N_r \sim r^{-5}$ for large bubbles—are identified in bubble size distribution. Moreover, rapid fluctuations in quantity over time can be observed for bubbles with a radius larger than 3 mm. These suggested that large bubbles and cavities are strongly related to air entrainment onset. The discovery is further proved by the spatial distribution of large bubbles, which corresponds well with the high local surface slope. Three air entrainment

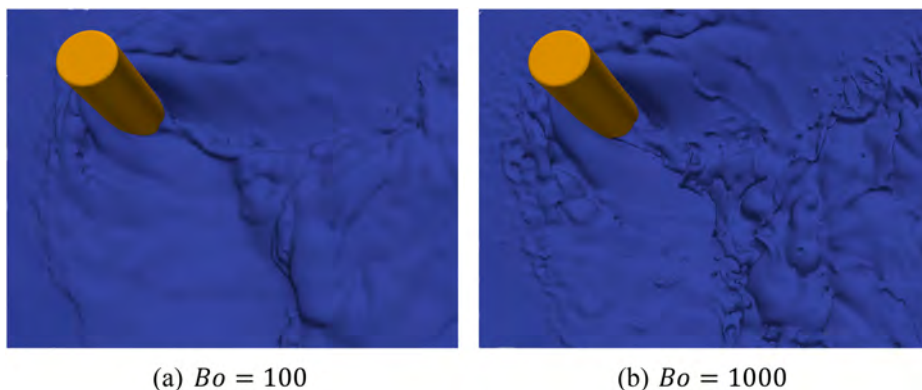


FIG. 29. Instantaneous free surface deformation in the depression region at $Bo = 100$ and 1000 .

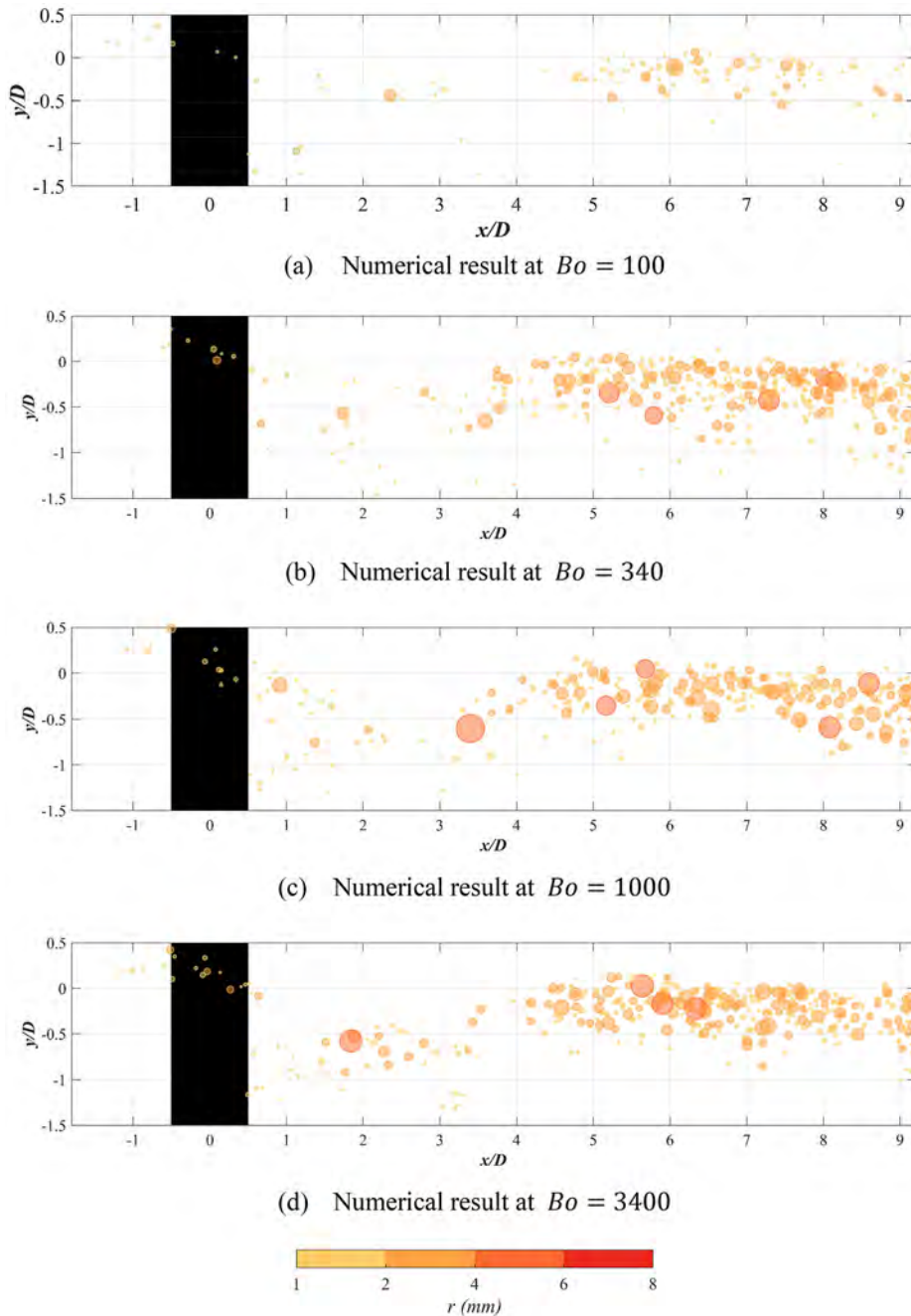


FIG. 30. Side view of the bubble spatial distribution at $Fr = 1.3$.

mechanisms are identified corresponding to the three distinct surface breaking regions. The instantaneous and time-accumulated bubble spatial distributions at various Froude numbers show a close relationship to the features of the velocity field. Moreover, surface tension effects on bubble statistics are examined. Low surface tension leads to more severe surface breaking and a larger number of bubbles, especially in the depression region.

ACKNOWLEDGMENTS

This work was supported by the National Natural Science Foundation of China (Grant No. 52131102), to which the authors are most grateful.

AUTHOR DECLARATIONS

Conflict of Interest

The authors have no conflicts to disclose.

Author Contributions

Wenbin Zhang: Data curation (equal); Formal analysis (equal); Investigation (equal); Methodology (equal); Software (equal); Validation (equal); Visualization (equal); Writing – original draft (equal). **Minghai Wang:** Data curation (equal); Formal analysis (equal); Investigation (equal); Validation (equal); Visualization (equal). **Weiwu Zhao:** Data curation (equal); Formal analysis (equal); Investigation (equal); Methodology (equal); Validation (equal); Writing – review & editing (equal). **Decheng Wan:** Conceptualization (equal); Funding acquisition (equal); Investigation (equal); Project administration (equal); Resources (equal); Software (equal); Supervision (equal); Writing – review & editing (equal).

DATA AVAILABILITY

The data that support the findings of this study are available from the corresponding author upon reasonable request.

REFERENCES

- ¹C. Norberg, “An experimental investigation of the flow around a circular cylinder: Influence of aspect ratio,” *J. Fluid Mech.* **258**, 287–316 (1994).
- ²A. Capone, C. Klein, F. Di Felice, and M. Miozzi, “Phenomenology of a flow around a circular cylinder at sub-critical and critical Reynolds numbers,” *Phys. Fluids* **28**(7), 074101 (2016).
- ³M. Ozgoren, “Flow structure in the downstream of square and circular cylinders,” *Flow Meas. Instrum.* **17**(4), 225–235 (2006).
- ⁴S. P. Singh and S. Mittal, “Flow past a cylinder: Shear layer instability and drag crisis,” *Int. J. Numer. Methods Fluids* **47**(1), 75–98 (2005).
- ⁵A. G. Kravchenko and P. Moin, “Numerical studies of flow over a circular cylinder at $Re_D=3900$,” *Phys. Fluids* **12**(2), 403–417 (2000).
- ⁶A. Travin, M. Shur, M. Strelets, and P. Spalart, “Detached-eddy simulations past a circular cylinder,” *Flow, Turbul. Combust.* **63**(1), 293–313 (2000).
- ⁷P. Catalano, M. Wang, G. Iaccarino, and P. Moin, “Numerical simulation of the flow around a circular cylinder at high Reynolds numbers,” *Int. J. Heat Fluid Flow* **24**(4), 463–469 (2003).
- ⁸Z. Liu, W. Zhao, and D. Wan, “CFD study of wave interaction with single and two tandem circular cylinders,” *Ocean Eng.* **239**, 109855 (2021).
- ⁹G. Wang, C. Zhang, F. Feng, C. Peng, and M. Zhang, “Water wave radiation by bottom-mounted surface-piercing concentric cylinders,” *Ocean Eng.* **297**, 116995 (2024).
- ¹⁰A. Hay, *Flow about Semi-Submerged Cylinders of Finite Length* (Princeton University, Princeton, NJ, 1947).
- ¹¹S. J. Keough, A. Ooi, J. Philip, and J. P. Monty, “Characterisation of flow regimes in the bow wave of a surface piercing cylinder,” *Appl. Ocean Res.* **145**, 103936 (2024).
- ¹²J. R. Chaplin and P. Teigen, “Steady flow past a vertical surface-piercing circular cylinder,” *J. Fluids Struct.* **18**(3), 271–285 (2003).
- ¹³G. Yu, E. J. Avital, and J. J. R. Williams, “Large eddy simulation of flow past free surface piercing circular cylinders,” *J. Fluids Eng.* **130**, 101304 (2008).
- ¹⁴B. Koo, J. Yang, S. M. Yeon, and F. Stern, “Reynolds and Froude number effect on the flow past an interface-piercing circular cylinder,” *Int. J. Naval Archit. Ocean Eng.* **6**(3), 529–561 (2014).
- ¹⁵M. A. Benitz, D. W. Carlson, B. Seyed-Aghazadeh, Y. Modarres-Sadeghi, M. A. Lackner, and D. P. Schmidt, “CFD simulations and experimental measurements of flow past free-surface piercing, finite length cylinders with varying aspect ratios,” *Comput. Fluids* **136**, 247–259 (2016).
- ¹⁶T. Kawamura, S. Mayer, A. Garapon, and L. Sørensen, “Large eddy simulation of a flow past a free surface piercing circular cylinder,” *J. Fluids Eng.* **124**(1), 91–101 (2002).
- ¹⁷S. J. Keough, I. Kermonde, A. Amiet, J. Philip, A. Ooi, J. Monty, and B. Anderson, “Time resolved measurements of wake characteristics from vertical surface-piercing circular cylinders,” in *Proceedings of the 20th Australasian Fluid Mechanics Conference*, Perth, Australia, 5–8 December 2016 (Australasian Fluid Mechanics Society, Perth, Australia, 2016).
- ¹⁸D. Potts, Z. Leong, J. Binns, H. Marcollo, and A. Skvortsov, “Wakes of surface-piercing cylinders,” in *Proceedings of ASME 2023 42nd International Conference on Ocean, Offshore & Arctic Engineering, OMAE2023* (American Society of Mechanical Engineers, New York, 2023), Vol. 5.
- ¹⁹V. Ageorges, J. Peixinho, and G. Perret, “Flow and air-entrainment around partially submerged vertical cylinders,” *Phys. Rev. Fluids* **4**(6), 064801 (2019).
- ²⁰V. Ageorges, J. Peixinho, G. Perret, G. Lartigue, and V. Moureau, “Experiments and simulations of free-surface flow behind a finite height rigid vertical cylinder,” *Fluids* **6**(10), 367 (2021).
- ²¹A. K. Hilo, J.-W. Hong, K.-S. Kim, B.-K. Ahn, G.-S. Lim, and S. Shin, “Experimental study on the flow patterns and acoustic characteristics of surface piercing cylinders,” *Ocean Eng.* **259**, 111895 (2022).
- ²²I. Eames and T. Robinson, “Free-surface channel flow around a square cylinder,” *J. Fluid Mech.* **980**, A16 (2024).
- ²³J. Suh, J. Yang, and F. Stern, “The effect of air–water interface on the vortex shedding from a vertical circular cylinder,” *J. Fluids Struct.* **27**(1), 1–22 (2011).
- ²⁴Z. Wang, J. Yang, and F. Stern, “A new volume-of-fluid method with a constructed distance function on general structured grids,” *J. Comput. Phys.* **231**(9), 3703–3722 (2012).
- ²⁵Z. Wang, J. Yang, B. Koo, and F. Stern, “A coupled level set and volume-of-fluid method for sharp interface simulation of plunging breaking waves,” *Int. J. Multiphase Flow* **35**(3), 227–246 (2009).
- ²⁶S. Chen, W. Zhao, and D. Wan, “Turbulent structures and characteristics of flows past a vertical surface-piercing finite circular cylinder,” *Phys. Fluids* **34**(1), 015115 (2022).
- ²⁷S. Chen, W. Zhao, and D. Wan, “Identification of vortical structures of flows past a surface-piercing finite square cylinder with rounded corners,” in *Liutex and Third Generation of Vortex Identification*, edited by Y. Wang, Y. Gao, and C. Liu (Springer Nature, Singapore, 2023), pp. 283–297.
- ²⁸M. S. Gritskevich, A. V. Garbaruk, J. Schütze, and F. R. Menter, “Development of DDES and IDDES Formulations for the $k-\omega$ shear stress transport model,” *Flow, Turbul. Combust.* **88**(3), 431–449 (2012).
- ²⁹P. R. Spalart, “Detached-eddy simulation,” *Annu. Rev. Fluid Mech.* **41**, 181–202 (2009).
- ³⁰J. Liu and C. Liu, “Modified normalized Rortex/vortex identification method,” *Phys. Fluids* **31**(6), 061704 (2019).
- ³¹D. Fuster and S. Popinet, “An all-Mach method for the simulation of bubble dynamics problems in the presence of surface tension,” *J. Comput. Phys.* **374**, 752–768 (2018).
- ³²S. Popinet, “Gerris: A tree-based adaptive solver for the incompressible Euler equations in complex geometries,” *J. Comput. Phys.* **190**(2), 572–600 (2003).
- ³³S. Popinet, “An accurate adaptive solver for surface-tension-driven interfacial flows,” *J. Comput. Phys.* **228**(16), 5838–5866 (2009).
- ³⁴M. Tavares, C. Josserand, A. Limare, J. M. Lopez-Herrera, and S. Popinet, “A coupled VOF/embedded boundary method to model two-phase flows on arbitrary solid surfaces,” *Comput. Fluids* **278**, 106317 (2024).
- ³⁵J. Li, “Calcul d’interface affine par morceaux,” *C. R. Acad. Sci.* **320**(8), 391–396 (1995).
- ³⁶E. Aulisa, S. Manservigi, R. Scardovelli, and S. Zaleski, “Interface reconstruction with least-squares fit and split advection in three-dimensional Cartesian geometry,” *J. Comput. Phys.* **225**(2), 2301–2319 (2007).
- ³⁷H. Johansen and P. Colella, “A cartesian grid embedded boundary method for poisson’s equation on irregular domains,” *J. Comput. Phys.* **147**(1), 60–85 (1998).
- ³⁸P. Schwartz, M. Barad, P. Colella, and T. Ligocki, “A Cartesian grid embedded boundary method for the heat equation and Poisson’s equation in three dimensions,” *J. Comput. Phys.* **211**(2), 531–550 (2006).
- ³⁹I. B. Celik, U. Ghia, P. J. Roache, and C. J. Freitas, “Procedure for estimation and reporting of uncertainty due to discretization in CFD applications,” *J. Fluids Eng.-Trans. ASME* **130**(7), 078001 (2008).
- ⁴⁰M. Rabaud and F. Moisy, “Ship wakes: Kelvin or Mach angle?,” *Phys. Rev. Lett.* **110**(21), 214503 (2013).
- ⁴¹F. Moisy and M. Rabaud, “Mach-like capillary-gravity wakes,” *Phys. Rev. E* **90**(2), 023009 (2014).
- ⁴²M. L. McAllister, S. Draycott, R. Calvert, T. Davey, F. Dias, and T. S. van den Bremer, “Three-dimensional wave breaking,” *Nature* **633**(8030), 601–607 (2024).

- ⁴³L. Deike, S. Popinet, and W. K. Melville, "Capillary effects on wave breaking," *J. Fluid Mech.* **769**, 541–569 (2015).
- ⁴⁴J. Jeong and F. Hussain, "On the identification of a vortex," *J. Fluid Mech.* **285**, 69–94 (1995).
- ⁴⁵Z. Wang, J. Yang, and F. Stern, "High-fidelity simulations of bubble, droplet and spray formation in breaking waves," *J. Fluid Mech.* **792**, 307–327 (2016).
- ⁴⁶W. Zhang, W. Zhao, and D. Wan, "Flow characteristics and bubble statistics during the fragmentation process of the ingested main cavity in plunging breaking waves," *J. Hydrodyn.* **36**(3), 546–555 (2024).
- ⁴⁷L. Deike, W. K. Melville, and S. Popinet, "Air entrainment and bubble statistics in breaking waves," *J. Fluid Mech.* **801**, 91–129 (2016).
- ⁴⁸X. Lu, T. Nie, X. Li, L. Jing, Y. Zhang, L. Ma, and D. Jing, "Insight into pH-controlled bubble dynamics on a Pt electrode during electrochemical water splitting," *Phys. Fluids* **35**(10), 103314 (2023).
- ⁴⁹W. Mostert, S. Popinet, and L. Deike, "High-resolution direct simulation of deep water breaking waves: Transition to turbulence, bubbles and droplets production," *J. Fluid Mech.* **942**, A27 (2022).
- ⁵⁰W. H. R. Chan, P. L. Johnson, P. Moin, and J. Urzay, "The turbulent bubble break-up cascade. Part 2. Numerical simulations of breaking waves," *J. Fluid Mech.* **912**, A43 (2021).
- ⁵¹G. B. Deane and M. D. Stokes, "Scale dependence of bubble creation mechanisms in breaking waves," *Nature* **418**(6900), 839–844 (2002).
- ⁵²X. Lu, T. Nie, D. Yadav, X. Li, Y. Zhang, L. Ma, and D. Jing, "Enhancing hydrogen bubble release from a microelectrode through precise tuning of Marangoni forces with nonionic surfactant," *Phys. Fluids* **36**(1), 013335 (2024).
- ⁵³X. Lu, D. Yadav, B. Ma, L. Ma, and D. Jing, "Rapid detachment of hydrogen bubbles for electrolytic water splitting driven by combined effects of Marangoni force and the electrostatic repulsion," *J. Power Sources* **599**, 234217 (2024).